Journal of Computational Physics 271 (2014) 281–305

Contents lists available at ScienceDirect

Journal of Computational Physics

www.elsevier.com/locate/jcp

Numerical treatment of wave breaking on unstructured finite volume approximations for extended Boussinesq-type equations

M. Kazolea [a], A.I. Delis [b,*], C.E. Synolakis [a]

[a] School of Environmental Engineering, Technical University of Crete, University Campus, Chania, Crete 73100, Greece
[b] School of Production Engineering & Management, Technical University of Crete, University Campus, Chania, Crete, Greece

ARTICLE INFO

Article history:
Received 21 May 2013
Received in revised form 12 November 2013
Accepted 18 January 2014
Available online 23 January 2014

Keywords:
Boussinesq-type equations
Wave breaking
Finite volumes
Unstructured meshes

ABSTRACT

A new methodology is presented to handle wave breaking over complex bathymetries in extended two-dimensional Boussinesq-type (BT) models which are solved by an unstructured well-balanced finite volume (FV) scheme. The numerical model solves the 2D extended BT equations proposed by Nwogu (1993), recast in conservation law form with a hyperbolic flux identical to that of the Non-linear Shallow Water (NSW) equations. Certain criteria, along with their proper implementation, are established to characterize breaking waves. Once breaking waves are recognized, we switch locally in the computational domain from the BT to NSW equations by suppressing the dispersive terms in the vicinity of the wave fronts. Thus, the shock-capturing features of the FV scheme enable an intrinsic representation of the breaking waves, which are handled as shocks by the NSW equations. An additional methodology is presented on how to perform a stable switching between the BT and NSW equations within the unstructured FV framework. Extensive validations are presented, demonstrating the performance of the proposed wave breaking treatment, along with some comparisons with other well-established wave breaking mechanisms that have been proposed for BT models.

1. Introduction

Mathematical and numerical modeling of non-linear wave transformations and their corresponding process has received much attention in the past few decades and has been one of the most interesting and active research fields in coastal engineering for simulating near-shore dynamics. Important issues one has to consider include, the validity of a mathematical model in near-shore zones as well as in deeper waters, representation of wave breaking, frequency dispersion and accurate numerical treatment of natural topographies and wetting/drying processes. Among these key issues, the natural phenomenon of wave breaking is of fundamental significance, playing a key role in the near-shore dynamics. In terms of the mathematical modeling, important physical effects associated with non-linear transformations of sea waves in near-shore regions can be described by Boussinesq-type (BT) equations. BT equations are more appropriate for describing flows in deeper waters where frequency dispersion effects may become more important than non-linearity. BT equations introduce dispersion terms in the modeling thus being more suitable in waters where dispersion begins to have an effect on the free surface.

Following from the seminal work of Boussinesq [12], the first set of extended BT equations was derived by Peregrine [51], under the assumption that non-linearity and frequency dispersion are weak and they are limited to relatively shallow

* Corresponding author.
E-mail addresses: mkazolea@isc.tuc.gr (M. Kazolea), adelis@science.tuc.gr (A.I. Delis).

0021-9991/$ – see front matter
http://dx.doi.org/10.1016/j.jcp.2014.01.030

water due to the weak dispersion. Subsequent attempts to extent the validity and applicability of these so-called standard Boussinesq equations have been successful. Madsen and Sørensen [46] and Nwogu [48] have extended their validity by giving a more accurate representation of the phase and group velocities in intermediate waters, closely relating to linear wave theory. Furthermore, significant effort has been made in recent years into advancing the non-linear and dispersive properties of BT models by including high order non-linear and dispersion terms, we refer for example to [8,28,40,9,10], among others, which in turn are more difficult to integrate and thus require substantially more computational effort in their numerical integration. For a very recent comprehensive review on the theory, numerics and applications of BT models we refer to the review work in [13].

Until recently, the predominant method for the numerical solution of BT equations was the finite difference (FD) method, we refer for example to [48,78,26,45,59] among many others. Finite volume (FV) methods have gained a lot of popularity the last few years. The application of the FV methodology to the BT equations is not straightforward due to the presence of the dispersive terms, therefore hybrid solutions, coupling the FV and the FD methods have been proposed for 1D BT equations, please refer, for example, in [25,11,17,35,56,42,59,60,63,10,69]. Further, this numerically hybrid approach has been extended to two space dimensions, for example in [38,72,71], but for uniform structured grids, restricting the modeling when dealing with 2D irregular geometries, similarly to the FD method. Asmar and Nwogu [24] proposed a FV scheme for Nwogu's BT equations [48] on unstructured meshes with a staggered placement of the variables. Recently Kazolea et al. [36] introduced, for the first time, the development and application of a conservative higher-order FV scheme for unstructured meshes, that exploits the advantages of the FV approach and incorporates state of the art discretizations for the topography and wet/dry front treatment.

Wave breaking has been incorporated into BT models by means of different artificial techniques. *The surface roller model* [58,43,44,64], *the vorticity model* and *the eddy viscosity model* [37,83,56,19,34] are three types of additional momentum dissipation methods. In *eddy viscosity* models dissipation due to turbulence generated by wave breaking and bore propagation is treated by a diffusion term in the momentum conservation equation in order to prevent numerical instabilities resulting from frequency and amplitude dispersion. The amount of dissipation is governed by the value of the eddy viscosity coefficient, which is expressed in terms of a mixing length parameter and is calibrated with experimental data, while a breaking criterion is used to decide exactly where and when the dissipation becomes active [20]. Heitner and Housner [31] proposed an eddy viscosity model to dissipate energy for breaking waves. Energy loss is limited to the front face of waves where the change of wave properties exceeds a certain criteria. Zelt [83] treated wave breaking similarly in a Lagrangian Boussinesq model to simulate solitary wave breaking and run-up. The same model used from Wei and Kirby [79]. Karambas and Koutitas [34] used also an eddy viscosity mechanism with the limitation that the formulation was not momentum preserving and the setup prediction in the inner surf zone (in the investigation of the performance for periodic waves) was very poor. Kennedy et al. [37] followed [31] and [83] but with extensions to provide a more realistic description of the initiation and cessation of wave breaking and were able to adequately reproduce wave height and setup for regular waves breaking on planar beaches. The largest disadvantage in that formulation is that, in some special cases, such as stationary hydraulic jumps, wave breaking initiation is not recognized. Additionally, Cienfuegos et al. [19] showed that Kennedy et al.'s eddy viscosity breaking model could hardly predict simultaneously accurate wave height and asymmetry along the surf zone. Lynett [41] used the eddy viscosity model of Kennedy et al. [37] with some modifications which regards the manner in which a breaking event is initiated and reformulations of the model's thresholds in terms of the total water depth H. Recently, Roeber et al. [56] adapt the approach of [31,37] and presented an eddy viscosity approach consistent with the conservative formulation of the BT equations of Nwogu [48] in 1D, to account for breaking waves in the surf zone.

Other methods are based on the *surface roller* concept introduced by Svendsen [66]. These methods, like the eddy viscosity ones, add a flux gradient to the BT momentum equation [58,64] but this approach stems from different hypothesis and ideas than those on the eddy viscosity ones. The added term depends on the dynamically determined roller thickness, the mean front slope of the breaker and other parameters which must be tuned during the numerical implementation. The roller approach has been improved by [43,44] and by [77,33]. Recently Cienfuegos et al. [17–19] considered the wave breaking energy dissipation through extra terms added both in mass and momentum equations.

The last few years, a new approach has emerged in which one simply (under certain conditions) turns off the dispersive terms in the region where breaking occurs, please refer to [71,72,55,35,11,9,69] among others. This formulation is based on the assumption that BT equations automatically degenerate into non-linear shallow water (NSW) equations as dispersive terms become negligible compared to non-linear terms. The idea introduced in [71–73], for the equations of Madsen and Sørensen [46], is to exploit the shock-capturing advantages of the FV scheme within the framework of BT modeling in order to simulate discontinuous phenomena such as wave breaking and run-up. More recently, the same rational was applied for a non-hydrostatic, near-shore wave model in [61]. These models take advantage of the fact that in shallow water, the NSW equations (under the FV framework) have the ability to naturally embody bore propagation and the related energy dissipation. This feature is interesting because of the similarity between spilling breakers and bores [52,5]. Borthwick et al. [11] introduced the above idea using as an indicator criterion one similar to the criterion used by Kennedy et al. [37]. In [71,72] a simple criterion (developed on a physical basis) introduced in the numerical scheme to establish which set of equations should be solved in each computational cell and recently they applied an extended version of their hybrid model, including an additional criterion for the switch back to the BT equations, to describe the transformation of irregular waves [74]. Roeber et al. [55] utilize the local momentum gradients as an indicator for deactivation of the dispersive terms. Among the works that have followed similar reasoning are also [69,9,59,11,50,10]. However, the treatment proposed in all

of these works have been developed for 1D and 2D BT equations on structure meshes. In addition, in almost all aforementioned works it is not clear the way that these wave breaking techniques can be implemented in two-dimensional schemes, especially unstructured ones, with a concern about each method's sensitivity to grid spacing [59].

In [36] the unstructured well-balanced FV scheme, developed for the solution of Nwogu's extended BT model, was applied only in simulating non-breaking wave propagation. In the present work, the FV model is extended and completed as to incorporate a proper treatment of wave breaking processes. The proposed wave breaking modeling is based on a hybrid approach where the dispersion terms in the BT model are suppressed under certain criteria and the NSW equations are used to govern the breaking process. A novel implementation of certain criteria is established to characterize the initiation and termination of the wave breaking process, along with a proposed methodology for switching between the two models within the FV framework. In addition, the application and performance of an eddy viscosity breaking model within this FV framework is presented.

The rest of the paper is organized as follows. Section 2 outlines the governing equations of the BT model. Section 3 reviews, in some detail, the unstructured FV numerical scheme proposed in [36]. In Section 4 the development of the proposed wave breaking treatment is presented along with some other approaches that, and for comparison purposes, have been implemented to treat breaking waves. Finally, in Section 5, the performance of the proposed methodology is extensively validated against experimental measurements from a series of relevant benchmark problems.

2. The extended Boussinesq-type equations

The model equations solved in the present work are the extended BT equations derived by Nwogu [48] using the velocity vector $[u,v]^{\mathrm{T}}=\mathbf{u}\equiv\mathbf{u}_a$ at an arbitrary distance, z_a, from a still water level, h, as the velocity variable, instead of the commonly used depth-averaged velocity. An optimum value of $z_a=-0.531h$ was derived so that the dispersion properties of the equations most closely approximate those defined by linear wave theory, making the equations applicable to a wider range of water depths, compared to the classical Boussinesq equations. The equations of Nwogu describe weakly non-linear and weakly dispersive water waves in variable water depth and were derived under the assumption that the wave height (A) to constant water depth (h) ratio, $\epsilon:=A/h$, which measures the weight of non-linear effects, and the square water depth to wave length (L) ratio $\mu^2:=h^2/L^2$, which represents the dimension of the dispersive effects, is of the same order with, i.e. the Stokes number $S:=\epsilon/\mu^2=O(1)$. The equations provide accurate linear dispersion and shoaling characteristics for values of kh up to 3 (intermediate water depths), where k is the wave number and kh is essentially a scale of the value of μ, providing a correction of $O(\mu^2)$ to the shallow water theory. By retaining $O(\mu^2)$ terms in the derivation of the models some vertical variations in the horizontal velocity are included even though the explicit appearance of the vertical coordinate has been removed from the continuity and momentum equations by integration.

The equations are presented here in a conservative-like form and as such are numerically approximated by an unstructured FV scheme. Following [36] the vector quasi-conservative form of the equations reads as:

$$\partial_t\mathbf{U}+\nabla\cdot\mathcal{H}\left(\mathbf{U}^{\star}\right)=\mathbf{S}\quad\text{on }\Omega\times[0,t]\subset\mathbb{R}^2\times\mathbb{R}^+,\tag{1}$$

where $\Omega\times[0,t]$ is the space–time Cartesian domain over which solutions are sought, $\mathbf{U}^{\star}=[H,Hu,Hv]^{\mathrm{T}}$ are the physically conservative variables, $\mathbf{U}$ is the vector of the actual solution variables and $\mathcal{H}=[\mathbf{F},\mathbf{G}]$ are the non-linear flux vectors given as

$$\mathbf{U}=\begin{bmatrix}H\\P_1\\P_2\end{bmatrix},\qquad\mathbf{F}=\begin{bmatrix}Hu\\Hu^2+\frac{1}{2}gH^2\\Huv\end{bmatrix},\qquad\mathbf{G}=\begin{bmatrix}Hv\\Huv\\Hv^2+\frac{1}{2}gH^2\end{bmatrix},$$

where the auxiliary variables

$$\mathbf{P}=\begin{bmatrix}P1\\P2\end{bmatrix}=H\left[\frac{z_a^2}{2}\nabla(\nabla\cdot\mathbf{u})+z_a\nabla(\nabla\cdot h\mathbf{u})+\mathbf{u}\right].\tag{2}$$

$H(\mathbf{x},t)=\eta(\mathbf{x},t)+h(\mathbf{x})$ is the total water depth (with $\eta(\mathbf{x},t)$ being the free surface elevation) and $h(\mathbf{x})$ the depth below the still water level. The source term vector, $\mathbf{S}=\mathbf{S_b}+\mathbf{S_f}+\mathbf{S_d}$, includes the bed topography's ($b(\mathbf{x})$) slope $\mathbf{S_b}$, the bed friction effects $\mathbf{S_f}$, given in this work in terms of the Manning coefficient n_m, and the dispersive terms $\mathbf{S_d}$. These terms read as

$$\mathbf{S_b}=\begin{bmatrix}0\\-gH\partial_x b\\-gH\partial_y b\end{bmatrix},\qquad\mathbf{S_d}=\begin{bmatrix}-\psi_c\\-u\psi_c+\psi_{M_x}\\-v\psi_c+\psi_{M_y}\end{bmatrix}\quad\text{and}\quad\mathbf{S_f}=\begin{bmatrix}0\\-gn_m^2u\|\mathbf{u}\|h^{-1/3}\\-gn_m^2v\|\mathbf{u}\|h^{-1/3}\end{bmatrix},$$

with

$$\psi_c=\nabla\cdot\left[\left(\frac{z_a^2}{2}-\frac{h^2}{6}\right)h\nabla(\nabla\cdot\mathbf{u})+\left(z_a+\frac{h}{2}\right)h\nabla(\nabla\cdot h\mathbf{u})\right],\tag{3}$$

$$\boldsymbol{\psi}_{\mathbf{M}}=\begin{bmatrix}\psi_{M_x}\\\psi_{M_y}\end{bmatrix}=\partial_t H\frac{z_a^2}{2}\nabla(\nabla\cdot\mathbf{u})+\partial_t Hz_a\nabla(\nabla\cdot h\mathbf{u}).\tag{4}$$

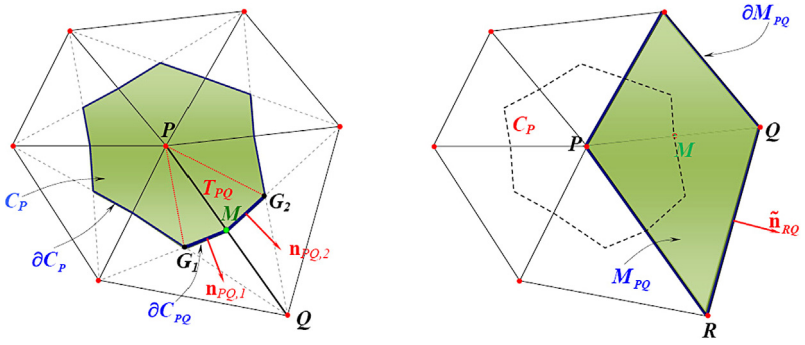

Fig. 1. Median-dual control cell definition (left) and computational cell for the gradient of the divergence (right).

Eqs. (1) have flux terms identical as those in the NSW equations and variables $\mathbf{P}$ contain all time derivatives in the momentum equations, including part of the dispersion terms. The dispersion vector $\mathbf{S_d}$ contains only spatial derivatives since $\partial_t H$ is explicitly defined by the mass equation. It is obvious that the NSW equations are a subset of the BT equations since Eqs. (1) degenerate into the NSW equations when the dispersive terms in $\mathbf{P}$ and $\mathbf{S_d}$ are vanishing.

3. The FV numerical scheme

To numerically solve (1), the FV numerical scheme proposed in [36] was implemented and we will review it here, for completeness. The considered FV approach is of the node-centered median-dual type, where the control volumes are elements dual to a primal triangular mesh $\mathcal{T}^{h_N}$, with h_N being the effective mesh size. The locations of the discrete solutions are called data points, N. Referring to Fig. 1, the boundary ∂C_P of a control volume, C_P, around an internal node P, is defined by connecting the barycenters of the surrounding triangles (having P as a common vertex) with the mid-points of the corresponding edges that meet at node P. The control volume's boundaries are called faces and the term edge refers to the line connecting the neighboring vertices. We also define $\partial C_{PQ} = \partial C_P \cap \partial C_Q$, M as the midpoint of edge PQ and the outward normal vector to ∂C_{PQ} as $\mathbf{n}_{PQ} = [n_{PQx}, n_{PQy}]^{\mathrm{T}}$, while $\tilde{\mathbf{n}}_{PQ}$ is the corresponding unit vector. If $\mathbf{n}_{PQ,1}$ is normal to $\overline{G_1 M}$ and $\mathbf{n}_{PQ,2}$ is normal to $\overline{MG_2}$, then we can define as $\mathbf{n}_{PQ} = \mathbf{n}_{PQ,1} + \mathbf{n}_{PQ,2}$.

After integration of (1) over each computational cell and application of the Gauss divergence theorem the semi-discrete form of the scheme follows the usual FV formulation and reads as

$$\frac{\partial \mathbf{U}_P}{\partial t} = -\frac{1}{|C_P|}\sum_{Q\in K_P}\widetilde{\mathcal{F}}_{PQ} - \frac{1}{|C_P|}\widetilde{\mathcal{F}}_{P,\Gamma} + \frac{1}{|C_P|}\sum_{Q\in K_P}\left\{\iint_{C_P.}\mathbf{S}\,d\Omega\right\}, \tag{5}$$

where $\mathbf{U}_P$ is the volume-average value of the conserved-like quantities at a given time, $K_P := \{Q \in \mathbb{N} \mid \partial C_P \cap \partial C_Q \neq 0\}$ is the set of neighboring nodes to P, Γ is the boundary of the computational domain Ω and $\widetilde{\mathcal{F}}_{PQ}$ and $\widetilde{\mathcal{F}}_{P,\Gamma}$ are the numerical flux vectors across each internal and boundary face, respectively. Assuming a uniform distribution of $\mathcal{H}$ over ∂C_{PQ}, equal to its value at the midpoint M of edge PQ, these fluxes are approximated as

$$\widetilde{\mathcal{F}}_{PQ} = \oint_{\partial C_{PQ}} (\mathbf{F}\tilde{n}_x + \mathbf{G}\tilde{n}_y)\,dl \approx (\mathbf{F}\tilde{n}_x + \mathbf{G}\tilde{n}_y)_M \|\mathbf{n}_{PQ}\| = (\mathbf{F}n_{PQx} + \mathbf{G}n_{PQy})_M. \tag{6}$$

Although a one-point quadrature rule is used here the ideas presented next can be applied to high-order integration, e.g. using Gauss quadrature. To evaluate the product $\mathbf{F}n_{PQx} + \mathbf{G}n_{PQy}$ at M, a one-dimensional Riemann problem is assumed, between the left (L) and right (R) states existing at the two sides of M, defined by the vectors $\mathbf{U}^{\star L}_{PQ}$ and $\mathbf{U}^{\star R}_{PQ}$ respectively. The numerical fluxes (6) in (5) can be evaluated solving the Riemann problem at cell interfaces. In this work the approximate Riemann solver of Roe [54] was utilized.

The above scheme is only first-order accurate if a constant distribution of the physical variables is assumed in each cell C_P, i.e. $\mathbf{U}^{\star L}_{PQ} = \mathbf{U}^{\star}_{P}$ and $\mathbf{U}^{\star R}_{PQ} = \mathbf{U}^{\star}_{Q}$. For BT models higher-order accuracy of the first-order derivatives is required so that the truncation errors in the numerical scheme are smaller than the dispersion terms present in the model. The MUSCL methodology of van Leer [76] can be extended to node-centered unstructured formulations in order to reach higher-order spatial accuracy. This extension relies on the evaluation of the fluxes with extrapolated $\mathbf{U}^{\star R}_{PQ}$ and $\mathbf{U}^{\star L}_{PQ}$ at the midpoint M of edge PQ. Each component of the physical variables $\mathbf{W} = [H, u, v]$ and bed topography b are extrapolated using extrapolation gradients which are obtained using a combination of centered and upwind gradients [23,36,1,62] as to increase accuracy of the basic MUSCL reconstruction [23]. In that way, a third-order-accurate upwind-biased scheme is constructed, reducing the numerical dissipation introduced to the non-linear flux and produces accurate solutions for smooth flow conditions [36]. Further, in cases were the non-linearity prevails, so the dispersion terms are negligible (e.g. when the NSW equations are solved), the use of a slope limiting procedure is necessary in order to reduce oscillations that can be produced in the

presence of shocks. In this work, the edge-based non-linear slope limiter of Van Albada–Van-Leer is used [1,23,29,62,75]. Details for the applied MUSCL-type reconstruction can be found in [36].

Following [2–4], the average of the gradient $(\nabla w)_P$ in a cell, which is necessary for the higher-order reconstruction and for the discretization of the dispersion terms later on, is computed in the region Ω_P which is described by the union of all triangles which share the vertex P. Thus, for a node P it holds that

$$(\nabla w)_P = \frac{1}{|C_P|} \sum_{Q \in K_P} \frac{1}{2}(w_P + w_Q)\mathbf{n}_{PQ}\,. \tag{7}$$

The integral average of the divergence of the velocity vector is computed applying again the divergence theorem and by approximating the line integrals using the trapezoidal quadrature rule, [36], leading to

$$(\nabla \cdot \mathbf{u})_P = \frac{1}{|C_P|} \sum_{Q \in K_P} \frac{1}{2}(\mathbf{u}_P + \mathbf{u}_Q) \cdot \mathbf{n}_{PQ}\,. \tag{8}$$

3.1. Well-balancing, wet/dry front treatment and mass conservation

An upwind discretization approach for the bed topography source term is adopted to satisfy the so-called $\mathcal{C}$-property in hydrostatic (flow at rest) conditions [7,32,47]. The topography source term must be linearized in the same way and evaluated in the same Roe-average states as the flux terms. By defining $\widetilde{\mathbf{R}}$ as the usual Roe-average right eigenvector matrix of the fluxes's Jacobian and $\widetilde{\boldsymbol{\Lambda}}$ the diagonal average eigenvalue matrix, we get

$$\iint_{C_P} \mathbf{S_b}(\mathbf{U}^\star)\,d\Omega \approx \sum_{Q \in K_P} \left(\mathbf{S_b}^-_{PQ} + \mathbf{S}^\star_{\mathbf{b}}\big|_{PQ}\right) = \sum_{Q \in K_P} \left(\frac{1}{2}\left[\widetilde{\mathbf{R}}\left(\mathbf{I} - |\widetilde{\boldsymbol{\Lambda}}|\widetilde{\boldsymbol{\Lambda}}^{-1}\right)\widetilde{\mathbf{R}}^{-1}\widetilde{\mathbf{S}}_{\mathbf{b}}\right]_{PQ} + \mathbf{S}^\star_{\mathbf{b}}\big|_{PQ}\right), \tag{9}$$

where $\widetilde{\mathbf{S}}_{\mathbf{b}}$ is the face normal source term approximation and $\mathbf{S}^\star_{\mathbf{b}}|_{PQ}$ a correction term that must be added to the source term discretization to maintain the well-balancing for higher-order schemes [53,47,36], given as

$$\widetilde{\mathbf{S}}_{\mathbf{b}}|_{PQ} = \begin{pmatrix} 0 \\ -g\frac{H^L+H^R}{2}(b^R - b^L)n_{PQx} \\ -g\frac{H^L+H^R}{2}(b^R - b^L)n_{PQy} \end{pmatrix} \quad \text{and} \quad \mathbf{S}^\star_{\mathbf{b}}|_{PQ} = \begin{pmatrix} 0 \\ -g\frac{H^L+H_P}{2}(b^L - b_P)n_{PQx} \\ -g\frac{H^L+H_P}{2}(b^L - b_P)n_{PQy} \end{pmatrix}. \tag{10}$$

The above treatment holds the exact flow at rest solution if the computationally domain is totally wet, by providing an exact balance between the numerical flux and slope source terms, i.e. at a cell face $u = v = 0$ and $b^R - b^L = -(H^R - H^L)$.

However, in wet/dry fronts special considerations are needed to accurately model transition between wet and dry areas and maintain the high-order spatial accuracy and mass conservation. As identified in [53,23,36], and we briefly list here for completeness, the following issues have to be addressed:

- *Dry cell identification*. Computational cells with water depth $H < \epsilon_{wd}$ are considered as dry, where ϵ_{wd} is a tolerance parameter computed from grid geometrical quantities [53,23].
- *Conservation of flow at rest with dry regions*. A FV scheme has to satisfy the extended $\mathcal{C}$-property [16]. We redefine the bed elevation at the emerging dry cell following [22,14,47,23,15] to obtain an exact balance at the front between the bed slope and the hydrostatic terms for steady conditions.
- *Consisted depth reconstruction in dry regions*. In a wet/wet steady case, in each computational cell were the MUSCL reconstruction for b involves dry cells $(\nabla H)_P = -(\nabla b)_P$ must be enforced to maintain higher-order accuracy [23].
- *Flow in motion over adverse slopes*. For flow in motion and at wet/dry fronts we impose, temporarily, $\mathbf{u} = 0$ for the computation of the numerical fluxes and source terms, following [16,22,47].
- *Water depth positivity and mass conservation*. To avoid computing negative water depths in drying cells and to achieve absolute mass conservation, we follow treatments proposed in [14,39,23].

3.2. Discretization of the dispersion terms

The mass equation in (5) contains the integral average of the dispersive term ψ_C in the source term $\mathbf{S_d}$. To approximate this term, we use the divergence theorem, which leads to

$$\begin{aligned}(\psi_c)_P &= \frac{1}{|C_P|} \oint_{\partial C_P} \left[\left(\frac{z_a^2}{2} - \frac{h^2}{6}\right)h\nabla(\nabla \cdot \mathbf{u}) + \left(z_a + \frac{h}{2}\right)h\nabla(\nabla \cdot h\mathbf{u})\right] \cdot \widetilde{\mathbf{n}}\,dl \\ &= \frac{1}{|C_P|} \sum_{Q \in K_P} \left\{ \oint_{\partial C_{PQ}} \left[\left(\frac{z_a^2}{2} - \frac{h^2}{6}\right)h\nabla(\nabla \cdot \mathbf{u})\right] \cdot \widetilde{\mathbf{n}}\,dl + \oint_{\partial C_{PQ}} \left[\left(z_a + \frac{h}{2}\right)h\nabla(\nabla \cdot h\mathbf{u})\right] \cdot \widetilde{\mathbf{n}}\,dl \right\}\end{aligned}$$

$$\approx \frac{1}{|C_P|}\sum_{Q\in K_P}\left\{\left[\left(\frac{z_a^2}{2}-\frac{h^2}{6}\right)h\right]_M\left[\nabla(\nabla\cdot\mathbf{u})\cdot\mathbf{n}_{PQ}\right]_M+\left[\left(z_a+\frac{h}{2}\right)h\right]_M\left[\nabla(\nabla\cdot h\mathbf{u})\cdot\mathbf{n}_{PQ}\right]_M\right\}. \tag{11}$$

Like before, we have assumed a uniform distribution of the integrated quantities over ∂C_{PQ} equal to their values at the midpoint M of the edge PQ. The right-hand side terms in (11) require the evaluation of the gradient of the divergence of $\mathbf{u}$ and $h\mathbf{u}$ along the edge midpoints M. Hence, the evaluation of the gradient of a quantity w at M requires the definition of a new computational cell constructed by the union of the two triangles which share edge PQ (see Fig. 1, on the right). By denoting with $K_{PQ} := \{R\in\mathbb{N}\mid R \text{ is a vertex of } M_{PQ}\}$ we obtain

$$|M_{PQ}|(\nabla w)_M=\iint_{M_{PQ}}\nabla w\,d\Omega=\oint_{\partial M_{PQ}} w\tilde{\mathbf{n}}_{RQ}\,dl=\sum_{\substack{R,Q\in K_{PQ}\\ RQ\in\partial M_{PQ}}}\frac{1}{2}(w_R+w_Q)\mathbf{n}_{RQ}, \tag{12}$$

with $\mathbf{n}_{RQ}$ the vector normal to the edge RQ.

Next, for the dispersive source terms in the momentum equations we have

$$\frac{1}{|C_P|}\iint_{C_P}-\mathbf{u}\psi_c+\boldsymbol{\psi}_{\mathbf{M}}\,d\Omega=\frac{-\mathbf{u}_P}{|C_P|}\iint_{C_P}\psi_c\,d\Omega+\frac{1}{|C_P|}\iint_{C_P}\boldsymbol{\psi}_{\mathbf{M}}\,d\Omega. \tag{13}$$

The first term of the right-hand side of the equation is discretized as before in (11) and the second term takes the discrete form:

$$\begin{aligned}(\boldsymbol{\psi}_{\mathbf{M}})_P&=\frac{1}{|C_P|}\iint_{C_P}\boldsymbol{\psi}_{\mathbf{M}}\,d\Omega=\frac{1}{|C_P|}\iint_{C_P}\partial_t H\frac{z_a^2}{2}\nabla(\nabla\cdot\mathbf{u})+\partial_t H z_a\nabla(\nabla\cdot h\mathbf{u})\,d\Omega\\&\approx\left[\partial_t H\frac{z_a^2}{2}\right]_P\left[\nabla(\nabla\cdot\mathbf{u})\right]_P+[\partial_t H z_a]_P|C_P|\left[\nabla(\nabla\cdot h\mathbf{u})\right]_P,\end{aligned} \tag{14}$$

where the divergence $(\nabla\cdot\mathbf{u})_P$ and $(\nabla\cdot h\mathbf{u})_P$ are computed again using formula (7).

It should be noted here that, the use of the divergence theorem for the computation of ψ_c in (11), reduces the order of this dispersive differential operator (to second). The gradient and divergence discrete operators applied in (11) and (14) are actually obtained from a trapezoidal quadrature, [2], and we expect to be accurate up to second order, at least for linear problems. According to [78] second order approximations to second order derivatives is sufficient so that truncation errors in the numerical scheme are smaller than the dispersion terms present in the BT model.

3.3. Boundary conditions and the internal source function

In the presented FV approach, the degrees of freedom are located directly on the physical boundary. As such, boundary conditions based on mesh faces rather than mesh vertices where adopted. To this end, the weak formulation was used where the boundary condition was introduced into the residual through the modified boundary flux $\widetilde{\mathcal{F}}_{P,\Gamma}$ in (5). The idea of using the weak formulation to calculate the flux (and dispersion terms) at the boundary has been used here in the description of wall (solid) boundary conditions [36].

Absorbing boundaries have also been applied which should dissipate the energy of incoming waves perfectly, in order to eliminate non-physical reflections. In front of this kind of boundaries a sponge layer is defined. On this layer, the surface elevation was damped by multiplying its value by a coefficient $m(\mathbf{x})$ defined as [81]

$$m(\mathbf{x})=\sqrt{1-\left(\frac{\mathbf{x}-d(\mathbf{x})}{L_s}\right)^2} \tag{15}$$

where L_s is the sponge layer width and $d(\mathbf{x})$ is the normal distance between the cell center with coordinates $\mathbf{x}$ and the absorbing boundary. The sponge layer width should be $L\leqslant L_s\leqslant 1.5L$, i.e. the width of the sponge layer is proportional to the wave length. Thus, longer wave lengths require longer sponge layers.

Wave generation in the model is achieved by using an internal wave generation method. In [80], a source function for the generation of surface water waves was derived. This source function was obtained using Fourier transform and Green's functions to solve the linearized and non-homogeneous equations for Nwogu's BT equations. In the present model, this source function wave-making method is adopted in order to let the reflected waves outgo through the wave generator freely since the source function inside the numerical domain does not interact with the reflected waves, and the sponge layer is able to absorb both long and short waves.

To obtain a desired oscillation signal in the wave generating area, a source function $S(\mathbf{x},t)$ is added into the mass conservation equation at each time step, which is expressed as

$$S(\mathbf{x},t)=D^*\exp\left(-\gamma(x-x_s)^2\right)\sin(\lambda y-\omega t) \tag{16}$$

in which

$$\gamma = \frac{5}{(\delta L/4)^2} = \frac{80}{\delta^2 L^2}$$

where L is the wave length, ω the wave frequency, θ the wave incident angle, $\lambda(= k_y = k\sin\theta)$ the wave number in the y-direction, x_s is the location of the center of the wave-making area, δ is a parameter that influences the width $W = \delta L/2$ of the wave generator area and D^* is the source function's amplitude. For a monochromatic wave, D^* is defined as

$$D^* = \frac{2\sqrt{\gamma} A_0 \cos\theta(\omega^2 - \alpha_1 g k^4 h^3)}{\omega k\sqrt{\pi}\exp(-l^2/4\gamma)[1 - \alpha(kh)^2]}$$

where h is the still water level at the wave generation region, A_0 the wave amplitude, $l(= k_x = k\cos\theta)$ the wave number in the x-direction, $\alpha = -0.390$ and $\alpha_1 = \alpha + 1/3$.

3.4. Velocity field recovery computations

Concerning the time discretization, an optimal third order explicit Strong Stability-Preserving Runge–Kutta (SSP-RK) method was adopted [65,36] under the usual CFL stability restriction. After each time step in the RK scheme, the values of the velocities u, v must be extracted from the new solution variable $\mathbf{P} = [P_1 \;\; P_2]^{\mathrm{T}}$, from the momentum equation. The discretization of $\mathbf{P}$ results into a linear system $\mathbf{MV} = \mathbf{C}$ with $\mathbf{M} \in R^{2N\times 2N}$, $\mathbf{V} = [\mathbf{u}_1, \mathbf{u}_2, \ldots, \mathbf{u}_N]^{\mathrm{T}}$ and $\mathbf{C} = [\mathbf{P}_1, \mathbf{P}_2, \ldots, \mathbf{P}_N]^{\mathrm{T}}$. Matrix $\mathbf{M}$ is a sparse, mesh dependent and structurally symmetric. Keeping in mind that $\mathbf{u}$ is our unknown velocity vector at each mesh node, each two rows of the matrix correspond to a node $P \in \{1, 2, \ldots, N\}$ on the grid and for each such node equation (2) holds. Using (7) to discretize equation (2) and replacing the arithmetic average in Eq. (7) by the values at the midpoints M of the edges equation (2) reads as:

$$H_P\left[\frac{(z_a^2)_P}{2}\frac{1}{|C_P|}\sum_{Q\in K_P}(\nabla\cdot\mathbf{u})_M\mathbf{n}_{PQ} + \frac{(z_a)_P}{|C_P|}\sum_{Q\in K_P}(\nabla\cdot h\mathbf{u})_M\mathbf{n}_{PQ} + \mathbf{u}_P\right] = \mathbf{P}_P. \tag{17}$$

We compute $\nabla\cdot\mathbf{u}$ and $\nabla\cdot h\mathbf{u}$ at M using again the computational cell M_{PQ} and following [36] we get:

$$(\nabla\cdot\mathbf{u})_M = \frac{1}{|M_{PQ}|}\iint_{M_{PQ}}\nabla\cdot\mathbf{u}\,d\Omega = \frac{1}{|M_{PQ}|}\oint_{\partial T_{PQ}}\mathbf{u}\cdot\tilde{\mathbf{n}}\,dl \approx \frac{1}{|M_{PQ}|}\sum_{\substack{R,Q\in K_{PQ}\\ RQ\in\partial M_{PQ}}}\frac{1}{2}(\mathbf{u}_R + \mathbf{u}_Q)\cdot\mathbf{n}_{RQ} \tag{18}$$

for $(\nabla\cdot\mathbf{u})$ and a similar computation is performed for $(\nabla\cdot h\mathbf{u})$. After some calculations the sparse $2N\times 2N$ linear system to be solved can be presented in a compact form, as:

$$\frac{(z_a^2)_P}{2|C_P|}\sum_{Q\in K_P}(\mathbf{A}_Q\mathbf{u}_Q + \mathbf{A}_P\mathbf{u}_P) + \frac{(z_a)_P}{|C_P|}\sum_{Q\in K_P}(\mathbf{B}_Q\mathbf{u}_Q + \mathbf{B}_P\mathbf{u}_P) + \mathbf{I_2}\mathbf{u}_P = \frac{1}{H_P}\mathbf{P}_P, \quad P = 1,\ldots,N, \tag{19}$$

where the sub-matrices $\mathbf{A}_Q, \mathbf{A}_P, \mathbf{B}_Q, \mathbf{B}_P$, given in Appendix A, depend only on the geometric quantities $\mathbf{n}_{PQ}$ and area $|M_{PQ}|$, please refer also to Fig. 1.

The properties of the sparse matrix vary depending on the physical situation of each problem solved, the type of the grid used and the number of the nodes on the grid. The matrix was stored in the compressed sparse row (CSR) format of and linear system was solved using the Bi-Conjugate Gradient Stabilized method (BiCGStab) [57]. The ILUT pre-conditioner from SPARSKIT package [57] was implemented and the reverse Cuthill–McKee (RCM) algorithm [27] was also employed to reorder the matrix elements as to minimize the matrix bandwidth. Convergence to the solution was obtained in one or two steps for the test problems presented in following sections.

Remark 1. The way this linear system is constructed and solved is important for the proposed wave breaking treatment presented next. The system's matrix, and operators used in BiCGStab, are constructed at a preprocessing stage at the beginning of each simulation. As such, first its structure is stored in the CSR format and reordered. Then the pre-conditioner of the reordered matrix is computed at this preprocessing stage and subsequently utilized to solve the linear system at each time step. So the data structure of these operator cannot be changed during the time marching process in a numerical simulation.

4. Wave breaking modeling

Wave breaking is an important modeling issue in near-shore environments. It dissipates wave energy through the generation of turbulence, including substantial air entrainment. Since the wave's amplitude increases due to shoaling, the wave's front becomes vertical and the wave's crest overturns. BT equations are unable to describe this phenomenon and an additional mechanism is necessary. A wave breaking model for the BT equations requires two mechanisms to simulate the

breaking process numerically. The first one is a trigger mechanism related to the initiation and, possibly the termination, of the breaking process. The second mechanism is an energy dissipation mechanism.

Existing wave breaking trigger models can be classified, in the main, into (a) phase-averaged breaking models and (b) phase resolving breaking models. Phase-averaged trigger models include wave characteristics which are representative of one full phase of the wave. Their limited use to BT models is attributed to the necessity of an algorithm that separates individuals waves in order to obtain the wave characteristics such as, wave height and wave length. Extension of these parameterizations to 2D wave cases, and especially for unstructured numerical meshes remains a very difficult task. A review of these wave breaking criteria can be found in Okamoto et al. [49] and references therein.

On the other hand, phase-resolving models use information at certain locations of the wave. There exist mainly two types of phase-resolving wave breaking mechanisms related to the initiation and termination of the breaking process. The first one is controlled by the local slope angle [58] and the second by the vertical speed of the free surface elevation [37]. In the present work, we consider wave breaking criteria of the phase-resolving type and we propose a combination of trigger mechanisms which can be classified as to fall in between of the two aforementioned phase-resolving approaches (namely the local slope and vertical speed variations).

For the energy dissipation a local switch from the BT model to the NSW model can be performed when a wave is characterized as ready to break, by suppressing the dispersion terms. This approach allows for a natural treatment of breaking waves as shocks and we can take advantage of the shock capturing properties of the developed unstructured FV scheme. In addition, by making this decision, i.e. switching locally to NSW equations, we conserve mass and momentum across the wave front of waves characterized as breaking ones. Furthermore, this switching allows a spatial characterization of the computational domain to pre- and post-breaking areas and as such an accurate description of both non-breaking (governed by the BT model) and breaking waves (governed by the NSW model) transformations and treatment of shoreline motion. Such an approach leads to hybrid (one- and two-dimensional) BT-NSW models and has gained attention by several researchers in the past few years, please refer to [11,71,72,35,59,55,50,69,74].

In this work two different approaches are considered and tested here for numerically resolving the wave breaking problem within the unstructured FV framework, an eddy viscosity approach and a proposed hybrid BT-NSW one. The Kennedy et al. [37] eddy viscosity approach is implemented here, integrated consistently with the rest of FV scheme, for comparison purposes and is presented next for completeness.

4.1. Eddy viscosity wave breaking model

Following [37] the mass conservation equation in (1) remains unchanged while an eddy viscosity term, $\mathbf{S_{BR}}$, is added as a source term to the momentum conservation equations of the BT model in (1) which reads as,

$$\mathbf{S_{BR}} = \begin{bmatrix} 0 \\ R_{B_x} \\ R_{B_y} \end{bmatrix} = \begin{bmatrix} 0 \\ \nabla \cdot \widetilde{\mathbf{R}}_{B_x} \\ \nabla \cdot \widetilde{\mathbf{R}}_{B_y} \end{bmatrix} \tag{20}$$

with

$$\widetilde{\mathbf{R}}_{B_x} = \begin{bmatrix} \nu \partial_x (Hu) \\ \frac{\nu}{2}(\partial_y (Hu) + \partial_x (Hv)) \end{bmatrix} \quad \text{and} \quad \widetilde{\mathbf{R}}_{B_y} = \begin{bmatrix} \frac{\nu}{2}(\partial_y (Hu) + \partial_x (Hv)) \\ \nu \partial_y (Hv) \end{bmatrix}, \tag{21}$$

with the eddy viscosity given by

$$\nu = B \delta_B^2 H \partial_t \eta, \tag{22}$$

where η is the free surface elevation ($\eta = H - h$) and δ_B is a mixing length coefficient which, according to [37], takes values between 0.5 and 1.5 producing very similar results, with the value of 1.2 to give the best ones and is the value adopted also in the present work. Quantity B is a non-dimensional parameter which varies smoothly from 0 to 1 as to account for the initiation and termination of wave breaking and to avoid an impulsive start of breaking, computed as

$$B = \begin{cases} 1, & \partial_t \eta \geqslant 2 \partial_t \eta^\star \\ \frac{\partial_t \eta}{\partial_t \eta^\star} - 1, & \partial_t \eta^\star \leqslant \partial_t \eta \leqslant 2 \partial_t \eta^\star \\ 0, & \partial_t \eta \leqslant \partial_t \eta^\star \end{cases} \quad \text{with} \quad \partial_t \eta^\star = \begin{cases} \partial_t \eta^{(F)}, & t \geqslant T^\star \\ \partial_t \eta^{(I)} + \frac{t - t_0}{T^\star}(\partial_t \eta^{(F)} - \partial_t \eta^{(I)}), & 0 \leqslant t - t_0 \end{cases}$$

to account for the initiation and termination of the breaking procedure. The magnitude of $\partial_t \eta^\star$ decreases in time from some initial value $\partial_t \eta^{(I)}$ to a final value $\partial_t \eta^{(F)}$. $\partial_t \eta$ is computed using the approximation $\partial_t \eta = \frac{\eta^{n+1} - \eta^n}{\Delta t^{n+1}}$. $T^\star$ is the transition time and t_0 the time that breaking begins, for each node characterized as a breaking one i.e. these nodes with $\partial_t \eta \geqslant \partial_t \eta^{(I)}$. The values of $\partial_t \eta^{(I)}$ and $\partial_t \eta^{(F)}$ are case depended, with $0.3\sqrt{gh} \leqslant \partial_t \eta^{(I)} \leqslant 0.65\sqrt{gh}$ and $0.15\sqrt{gh} \leqslant \partial_t \eta^{(F)} \leqslant 0.4\sqrt{gh}$. For example, as was tested in [20] and confirmed in the present work, $\partial_t \eta^{(I)} = 0.35\sqrt{gh}$ for waves propagating on a barred beach and $\partial_t \eta^{(I)} = 0.65\sqrt{gh}$ for waves propagating on a monotone sloping beach. The transition time used here was set to $T^\star = 5\sqrt{h/g}$.

To discretize the breaking terms we follow the FV framework introduced up to now. Integrating the eddy viscosity terms over a computational cell C_P and applying the divergence theorem we obtain for the momentum equations:

$$(\mathbf{R_B})_P = \frac{1}{|C_P|}\iint_{C_P}\begin{bmatrix}\nabla\cdot\widetilde{\mathbf{R}}_{B_x}\\ \nabla\cdot\widetilde{\mathbf{R}}_{B_y}\end{bmatrix}d\Omega = \frac{1}{|C_P|}\sum_{Q\in K_P}\oint_{\partial C_{PQ}}\begin{bmatrix}\widetilde{\mathbf{R}}_{B_x}\cdot\tilde{\mathbf{n}}\\ \widetilde{\mathbf{R}}_{B_y}\cdot\tilde{\mathbf{n}}\end{bmatrix}dl \approx \frac{1}{|C_P|}\sum_{Q\in K_P}\begin{bmatrix}\widetilde{\mathbf{R}}_{B_x}\cdot\mathbf{n}_{PQ}\\ \widetilde{\mathbf{R}}_{B_y}\cdot\mathbf{n}_{PQ}\end{bmatrix}_M, \tag{23}$$

assuming, as before, a uniform distribution of $\widetilde{\mathbf{R}}_B\cdot\tilde{\mathbf{n}}$ over ∂C_{PQ} and equal to its value at the midpoint M of edge PQ.

The right-hand side terms in Eq. (23) requires the evaluation of $\widetilde{\mathbf{R}}_{B_x}$ and $\widetilde{\mathbf{R}}_{B_y}$ along the edge midpoints M. Hence, we use the computational cell M_{PQ} (referring again to Fig. 1). Formula (15) is used for the computation of the vectors $\nabla(Hu)$ and $\nabla(Hv)$, and consequently for the terms $\widetilde{\mathbf{R}}_{B_x}$ and $\widetilde{\mathbf{R}}_{B_y}$. The value of the eddy viscosity term at M, ν_M, is computed as the arithmetic average of the eddy viscosity values at nodes P and Q (ν_P and ν_Q respectively). Furthermore $\partial_t\eta$ which is necessary for the computation of ν_P and B is explicitly obtained from the mass equation.

4.2. Hybrid wave breaking model

In the last few years the hybrid BT-NSW approach has gained popularity due to its simplicity and efficiency. However, considerations still exist in the criteria chosen to characterize wave breaking, the proper switching between the BT equations and to the NSW ones, range of applicability and grid sensitivity. In addition, this approach has never been applied to unstructured meshes before the present work, to the best of our knowledge. In this approach we first estimate the location of breaking waves using explicit criteria and then the NSW equations are applied on the breaking regions and BT equations elsewhere. Tonelli and Petti in [71,72] and for the MS [46] BT model, developed a criterion which is based on the similarity between spilling breakers and moving hydraulic jumps, concluding this criterion to be the ratio of surface elevation to water depth, $\epsilon = \frac{\eta}{h}$. When a wave moves towards a beach, water depth decreases more rapidly than the wave length due to shoaling, so μ^2 decreases and ϵ increases. This wave breaking scheme is based on the assumption that BT equations degenerate into the NSW ones, as dispersive terms become negligible compared to the non-linear terms. Thus, the proposed numerical approach of [72] solves NSW equations in the region where non-linearity prevails and the BT equations elsewhere. The threshold value of the criterion used in order to establish which set of equations should be solved in each computational cell is set to 0.8. Also, in order to make the scheme more stable, once NSW equations have been applied, the ϵ value has to drop below 0.35–0.55 for BT equations to be applied again [74]. This approach has been proven successful in many applications, with its main advantage being its simplicity since no calibration parameters are needed, see [35,59,50] for example. However, the above criterion maybe proven inadequate, especially if waves propagate over a near-shore bar, when numerical wave breaking ceases before all the wave energy is dissipated. This is due to the static application of this breaking approach while a mechanism is needed that tracks propagating breaking fronts. In addition, all the applications of this criterion, thus far, have been restricted to 1D or 2D computations on structured meshes. This approach is also applied in this work and we name the model that utilizes this approach Hybrid(ϵ).

It should be stress here that, application of any hybrid approach to the unstructured FV scheme presented here is not straightforward and a special treatment is in need to perform a stable switch between the BT and NSW model which minimizes mesh dependence and stability issues on finer meshes.

4.2.1. Wave breaking criteria and the new hybrid model

An alternative hybrid model was presented in [11] for the Madsen and Sørensen [46] BT model, where it was assumed that wave breaking occurs when the vertical velocity component at the free surface exceeds a value proportional to the shallow water wave phase celerity, such that $\partial_t\eta > \gamma\sqrt{gh}$, where $0.35 \leqslant \gamma \leqslant 0.65$, is a calibration constant which maybe affected by the scale of the wave under consideration. A value of $\gamma = 0.3$ was used for breaking solitary waves on a sloping beach in [11]. In general, this criterion for breaking initiation is similar to one used by Kennedy et al. [37] and can be derived considering the non-linear advection equation for the free surface [20]. However, like Kennedy et al.'s eddy viscosity approach, this criterion is inefficient for stably computing stationary (breaking or partially breaking) hydraulic jumps since in these cases $\partial_t\eta \approx 0$.

In the light of the above mentioned works, we propose here the combination of two phase-resolving criteria for triggering wave breaking modeling within our FV scheme. Namely,

- the surface variation criterion: $|\partial_t\eta| \geqslant \gamma\sqrt{gh}$, with the value of $\gamma \in [0.3,\ 0.65]$ depending on the physical configuration, and
- the local slope angle criterion: $\|\nabla\eta\|_2 \geqslant \tan(\phi_c)$, where ϕ_c is the critical front face angle at the initiation of breaking.

The first criterion flags for breaking when $\partial_t\eta$ is positive, as breaking starts on the front face of the wave and has the advantage that can be easily calculated during the running of the model. The second criterion acts complementary to the first one and is based on the critical front slope approach in [58,64]. Depending on the BT model used and the breaker type, e.g. spilling or plunging, the critical slope values are in the range of $\phi_c \in [14°, 33°]$. For certain BT models this has been considered as the least sensitive breaking threshold, with the correct breaking location predicted for $\phi_c \approx 30°$, see for

example [41,69], and is the value adopted in this work. This value for ϕ_c is relatively large for this criterion to trigger by its own the breaking process, for different test cases, in our BT model but is sufficient to detect breaking hydraulic jumps thus, correcting the limitation of the first criterion.

In the numerical scheme and for each mesh node in the computational domain at every time step, we check if at least one of the above criteria is satisfied, and flag the relative node as a breaking or a non-breaking one. Then, each breaking wave, with its corresponding breaking mesh nodes, has to be identified. Thus, for each breaking wave we have to create a distinct dynamic list that contains all of its nodes characterized as breaking ones. To achieve this, and as such distinguish between different breaking waves, the following procedure is performed: a flagged breaking node is randomly chosen and its neighbors in the mesh data structure are identified. From these neighboring nodes we check which ones have been flagged as breaking ones and we add them to the list. We continue by following the same procedure for the next element in the list until we reach the last element on the list (for which its breaking neighboring nodes are already in the list).

Having distinguished the different breaking waves we can treat each wave individually and certain wave characteristics can be computed. The wave front of each breaking wave will be then handled as a bore by the NSW equations and as long as they are governed by these equations the shock will keep dissipating energy. However, we should take into account that bores stop breaking when their Froude number drops below a critical value. The wave's Froude number (Fr) determines the bore's shape and the transition from one kind of bore to another. If $Fr \gg 1$, a bore is purely breaking and will consist of a steep front and if the Froude number drops below a certain value Fr_c non-breaking undular bores have been observed, see [69] and references therein. Thus, an additional criterion is needed to determine when to switch back to the BT equations for non-breaking bores, allowing for the breaking process to stop. The criterion introduced by [69] is adopted here and is based on the analogy between a broken wave and a bore in the sense of a simple transition between two uniform levels. The wave's Froude number is defined as:

$$Fr = \sqrt{\frac{(2H_2/H_1 + 1)^2 - 1}{8}}, \tag{24}$$

where H_1 is the water depth at the wave's trough and H_2 the water depth at the wave's crest. Since we have tracked each breaking wave individually (with its own dynamic list), it is relatively straightforward to find H_1 and H_2 for each wave. We simply approximate them by finding the minimum and maximum water depth respectively, from all the breaking nodes corresponding to that wave. If $Fr \leqslant Fr_c$ all the breaking points of that wave are un-flagged and the wave is considered non-breaking. Following [69] the critical value for Fr_c was set equal to 1.3 in our computations.

For each breaking wave, the computational region along the wave direction, l_{NSW}, is defined as $[x_{\min}, x_{\max}] \times [y_{\min}, y_{\max}]$, where $x_{\min}$ and $x_{\max}$ is the breaking node's minimum and maximum x-coordinate respectively. Similarly for $y_{\min}, y_{\max}$. This region over which we switch to NSW equations is roughly centered around the wave front. However, non-physical effects may appear at the interface between a zone that is governed by the BT equations and a zone that is governed by the NSW model, due to the relatively strong variations that may exist in the solution, which affect the estimation of the dispersive terms [50,69,59]. In [69] the shallow water region was extended assuming that the l_{NSW} length must be larger than the order of magnitude of the physical length of the wave roller. The length of the roller can be defined as $l_r \approx 2.9(H_2 - H_1)$ and the extend $l_{NSW} \approx 2.5 l_r$, which is the value adopted in the present work. Then, the new NSW region is $[x_{\min} - \delta_x,\ x_{\max} + \delta_x] \times [y_{\min} - \delta_y,\ y_{\max} + \delta_y]$, where $\delta_x = \max(2.5l_r - (x_{\max} - x_{\min}), 0)$ and $\delta_y = \max(2.5l_r - (y_{\max} - y_{\min}), 0)$.

The methodology to handle wave breaking can be summarized as follows:

1. Computation of wave breaking criteria for each computational cell.
2. If at least one of the criteria is satisfied, flag the relative nodes as breaking ones.
3. Distinguish different breaking waves by creating a dynamical list that contains the breaking nodes of such a wave.
4. Computation of certain waves' characteristics such as, wave height and Froude number.
5. Switch back to the BT equations for non-breaking undular bores, if $Fr < Fr_c$.
6. For each breaking wave, extension of the computational region governed by the NSW equations.

4.2.2. Suppression of the dispersive terms methodology

After the characterization of the breaking regions the NSW model has to be applied computationally in each one of them. This means that all dispersive terms, ψ_c and $\boldsymbol{\psi}_{\mathbf{M}}$ in (1) have to be suppressed at mesh nodes triggered as breaking ones. Several researchers have followed similar approach in their hybrid models, we refer to [71,72,74,55,59,10] for 2D applications. In the aforementioned works, a FV/FD approach has been adopted on structured meshes. The corresponding two linear systems produced (along the x- and y-direction respectively) for the velocity field recovery (see Section 3.4) are tridiagonal ones which can be more easily adapted in time since the equations corresponding to breaking nodes theoretically must be as those in the identity matrix, since the dispersive terms are suppressed. However, in [71] and [55] it was state that the matrices where precalculated and used throughout the computations. As we stated in Remark 1, also for our unstructured solver the matrix of the linear system cannot be changed due to its storage in the compressed sparse row (CSR) format. Any change in the matrix structure through time marching would result in a large increase in the computational cost. Furthermore, is not clear how the switching between the two models is implemented, with an additional concern for issues of sensitivity to grid spacing. According to [59] there is a discontinuity at the switching point between the BT equations and

NSW ones. This discontinuity is introduced to the dispersive terms of the BT equations causing spurious oscillations at the switching points. The frequency of these oscillations increases with grid refinement, producing instabilities.

For the above reasons there is the need of a robust and efficient implementation of the switching procedure. A methodology to stably handle the switching between the two models is developed within the unstructured FV framework of the present work and is detailed below:

0. Starting with the solution vector $\mathbf{U}_P^n$, $P = 1, \ldots, N$, at time t^n,
1. For all computational cells an $[H_1^{n+1}, H_2^{n+1}, \ldots, H_N^{n+1}]^{\mathrm{T}}$ solution is computed from the mass equation using the BT model (named from now on $\mathbf{H}_{BT}^{n+1}$ solution).
   1.1 If breaking has been activated (according to our criteria) for a number of computational cells say $N_{br} < N$, an additional solution vector is computed by subtracting the dispersive terms ψ_c from $\mathbf{H}_{BT}^{n+1}$ at these breaking cells, i.e. obtaining a NSW solution for $\mathbf{H}^{n+1}$ at these cells only. This solution is named $\mathbf{H}_{BT/SW}^{n+1}$ from now on.
2. Then, for all computational cells the $\mathbf{P}_{BT}^{n+1} = [\mathbf{P}_1^{n+1}, \mathbf{P}_2^{n+1}, \ldots, \mathbf{P}_N^{n+1}]_{BT}^{\mathrm{T}}$ solution from the momentum equation is computed, using the approximation $\partial_t \mathbf{H}^{n+1} \approx \frac{\mathbf{H}_{BT}^{n+1} - \mathbf{H}^n}{\Delta t^{n+1}}$ for the $\psi_{\mathbf{M}}$ computation in (4).
   2.1 If breaking has been activated for a number of computational cells, an additional solution (named $\mathbf{P}_{BT/SW}^{n+1}$) is computed by subtracting the dispersive terms ψ_c and $\boldsymbol{\psi}_{\mathbf{M}}$ from $\mathbf{P}_{BT}^{n+1}$ at these cells i.e. obtaining a NSW momentum solution $[(Hu)^{n+1},\ (Hv)^{n+1}]^{\mathrm{T}}$ for the breaking cells, since for the NSW equations $\mathbf{P} = [P_1,\ P_2]^{\mathrm{T}} = [Hu,\ Hv]^{\mathrm{T}}$. For theses cells only it is easy now to compute $\mathbf{u}_{SW}^{n+1} = [\mathbf{u}_1^{n+1}, \ldots, \mathbf{u}_{N_{br}}^{n+1}]_{SW}^{\mathrm{T}}$ which will be a subset of the actual velocity solution sought.
3. Then, the linear system $\mathbf{MV} = \mathbf{C}$ from (18) is solved with $\mathbf{C} = [\mathbf{P}_1^{n+1}, \mathbf{P}_2^{n+1}, \ldots, \mathbf{P}_N^{n+1}]_{BT}^{\mathrm{T}}$ to obtain an approximation of the velocity vector, named $\mathbf{u}_{BT}^{n+1} = [\mathbf{u}_1^{n+1}, \ldots, \mathbf{u}_N^{n+1}]_{BT}^{\mathrm{T}}$.
4. The final solution at $t = t^{n+1}$ will be that of $\mathbf{H}_{BT/SW}^{n+1}$ for the total water depth and $\mathbf{P}_{BT/SW}^{n+1}$ for the momentum equations. For the velocity field vector the solution, denoted as $\mathbf{u}_{BT/SW}^{n+1}$, is derived from the $\mathbf{u}_{BT}^{n+1}$ vector with its values at the breaking nodes replaced by those of $\mathbf{u}_{SW}^{n+1}$.

Remark 2. It is important to note here that, at steps 1 and 2 in the above algorithm, where solutions for $\mathbf{H}_{BT}^{n+1}$ and $\mathbf{P}_{BT}^{n+1}$ are obtained, the advective part of the FV scheme uses values $\mathbf{W}_{BT/SW}^n = [H^n,\ u^n,\ v^n]_{BT/SW}^{\mathrm{T}}$, i.e. hybrid values, while for the dispersive part discretization, the $\mathbf{W}_{BT}^n = [H^n,\ u^n,\ v^n]_{BT}^{\mathrm{T}}$ values are used. In this way at the switching nodes the use of non-smooth solutions is avoided on the approximation of the dispersive terms.

With the above treatment no non-physical discontinuity is introduced to the Boussinesq-type equations and no non-physical mix of both set of equations is performed in the solution of the linear system. We point here that the above procedure has been developed for the higher-order explicit time marching scheme implemented in this work. If an implicit time marching scheme is to be adopted, we conjecture that, the ideas presented can be carried over but its implementation would be different and modifications maybe needed in the procedure. This is a topic that can be benefit from further research.

5. Numerical tests and results

5.1. Solitary wave run-up on a plane beach

Solitary wave run-up on a plane beach is one of the most intensively studied problems in long-wave modeling. Synolakis [68] carried out laboratory experiments for incident solitary waves of multiple relative amplitudes, in order to study propagation, breaking and run-up over a planar beach with a slope 1:19.85. Many researchers have used this data set to validate numerical models, we refer to [83,42,9,72,21,56,55,19,82,70] among many others. With this test case we asses the ability of our model to describe shoreline motions and wave breaking, when it occurs. According to Synolakis [68] wave breaking occurs during run-down when $A/h > 0.044$. The incident wave height for the case considered here is $A/h = 0.28$, so the wave broke strongly both in the run-up and the run-down phases of the motion. The initial surface profile for η and velocity $\mathbf{u}$ (with $v = 0$) was computed with the semi-analytical solution from [78]. A Manning coefficient of $n_m = 0.01$ was used to define the glass surface roughness used in the experiments. We consider a computational domain of $(x, y) \in [-20, 60\ \mathrm{m}] \times [0, 0.8\ \mathrm{m}]$. The numerical model used a triangular grid consisting of triangles with side length of $h_N = 0.05$ m leading to a mesh of $N = 30,428$ nodes, the CFL number was set equal to 0.35 and a sponge layer is applied offshore with length $L_s = 5$ m. For the surface variation breaking criterion, $\partial_t \eta \geqslant \gamma\sqrt{gh}$, γ was set equal to 0.6. The wet/dry threshold value was set as $\epsilon_{wd} = 1.d - 6$.

Figs. 2 and 3 compare the measured surface profiles and the numerical model's results on different non-dimensional times. Numerical results using the eddy viscosity model, using $\partial_t \eta^{(I)} = 0.55\sqrt{gh}$ and $\partial_t \eta^{(F)} = 0.15\sqrt{gh}$, are simultaneously presented. Until time $t\sqrt{g/h} = 10$ the solitary propagates to the shore and the two models produce, as expected, identical

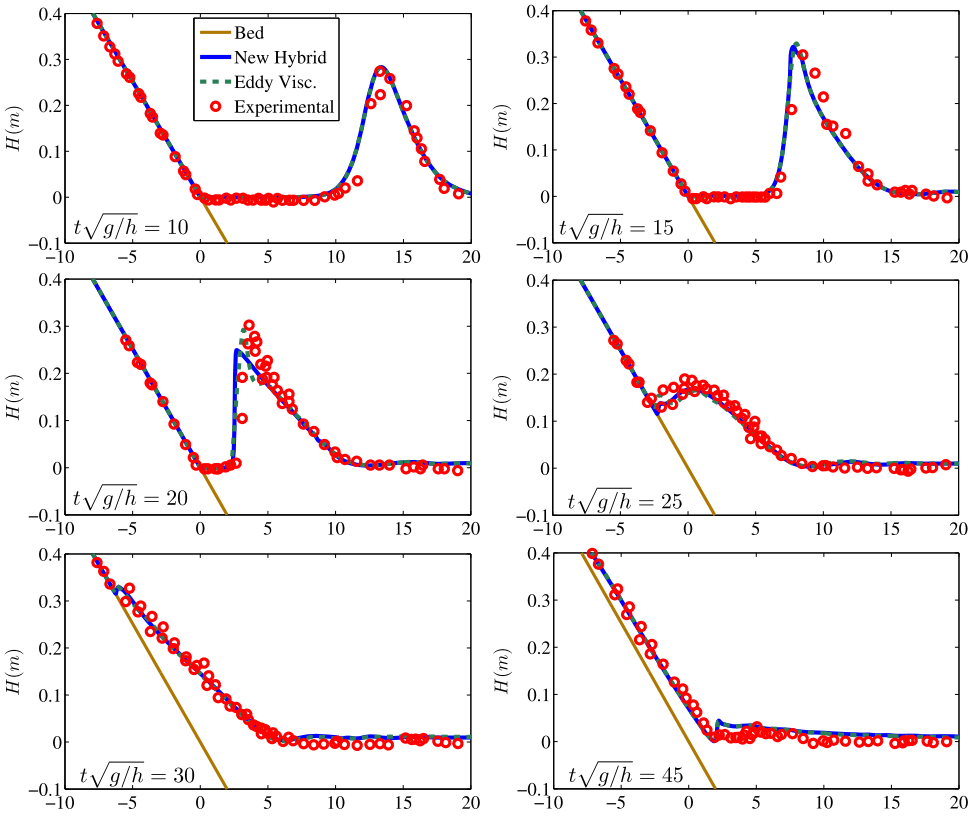

Fig. 2. Free surface elevation of solitary wave run-up on a plane beach for $A/h = 0.28$ (cont).

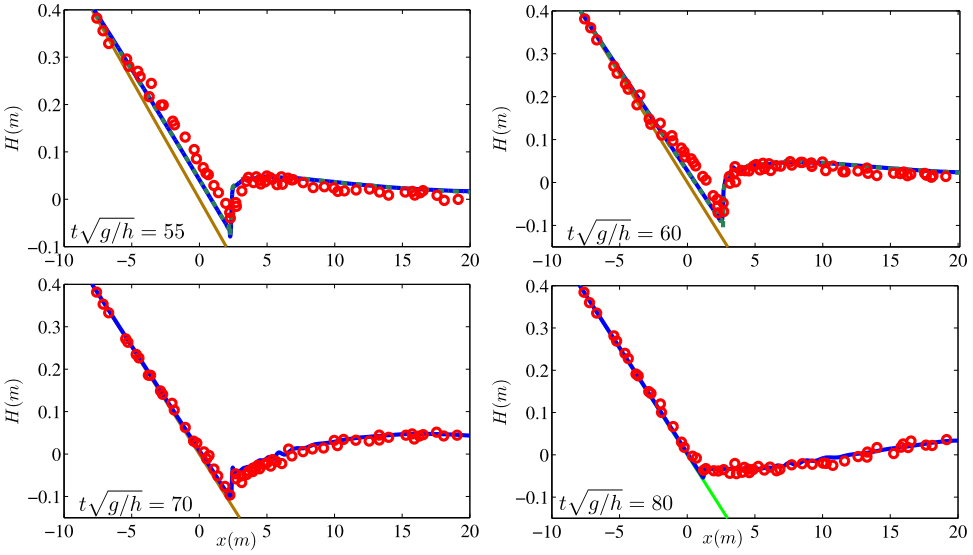

Fig. 3. Free surface elevation of solitary wave run-up on a plane beach for $A/h = 0.28$.

results since wave breaking hasn't started yet. The experimental wave breaks around $t\sqrt{g/h} = 20$. The numerical solution for the new hybrid model is represented like a bore storing the water spilled from the breaking wave behind the front. We can see the differences in the two solutions at time $t\sqrt{g/h} = 20$. In the eddy viscosity model the wave breaking is simulated as a triangular bore. Similar behavior has been observed by other researchers too [83,19,42]. At time $t\sqrt{g/h} = 25$ the bore collapses at the shore and the results show good qualitative agreement except the front face of the bore which is due to the different bore head at the breaking time. After that the wave starts to run-up. The time of maximum run-up occurs at

Table 1
Experimental wave characteristics for the Hansen and Svendsen tests [30].

Test	T (s)	H (m)	S	Breaking type
031041	3.333	0.043	17.5588	Plunging
051041	2.0	0.036	4.8077	Spilling

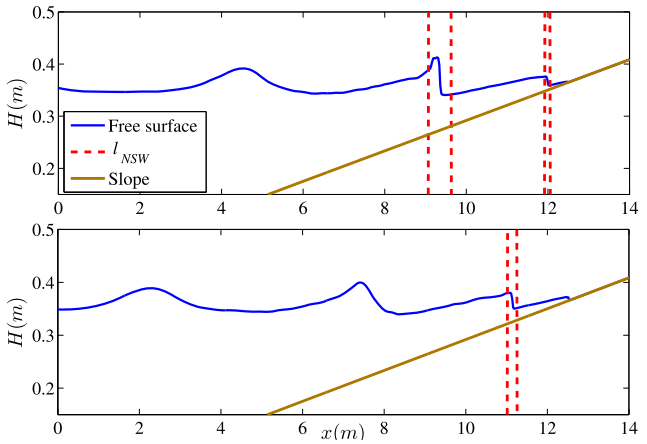

Fig. 4. Spatial snapshots along the centerline of regular waves over a sloping beach with the flow between two consecutive vertical lines governed by the NSW equations.

$t\sqrt{g/h} = 45$. Up to that time the computed solution fully recovers due to the volume conservation in both models. As the water recedes a breaking wave is created at $t\sqrt{g/h} = 55$ near the still water level. The numerical solution is approximated as a hydraulic jump. According to Kennedy et al. [37] the largest disadvantage of the eddy viscosity model is that, in some cases, such as stationary hydraulic jumps, breaking initiation is not recognized. For that reason oscillations at the numerical solution of the eddy viscosity model where observed after $t\sqrt{g/h} = 55$ and the solution became unstable. Thus, no results for this model are include in Fig. 3 for times $t\sqrt{g/h} = 70$ and $t\sqrt{g/h} = 80$. Zelt [83] has also mentioned that it might also be necessary to treat that backwash bore by a completely different breaking algorithm in place of the artificial viscosity model. On the other hand, the new hybrid breaking model has better agreement with the experimental data, with no stability problems observed, due to the local slope angle criterion utilized complementary to the surface variation criterion that explicitly detects the formation of the hydraulic jump which is resolved by the NSW model.

5.2. Regular waves breaking on a sloping beach

Hansen and Svendsen [30] performed a number of regular wave test on plane slopes in order to study wave shoaling and breaking on a sloping beach. Waves were generated over a 0.36 m horizontal bottom, propagated shoaled and broke over a slope of 1:32.26. Multiple tests were performed including plunging breakers and spilling breakers and many authors have used the experimental data for model validation. We refer for example to [37,72,59,34,19,77]. Two of these experiments, producing breaker types of a strong plunging and spilling, are recreated numerically in this work and are described in Table 1. We denote T the wave period, H the incident wave height and S the corresponding Stokes number. The computational domain is 52 m long and 1 m wide were $(x, y) \in [-26, 26\text{ m}] \times [0, 1\text{ m}]$. For the computation a triangular grid was used, consisting of equilateral triangles with side length $h_N = 0.025$, leading to a mesh of $N = 49{,}956$ nodes. The CFL value used was 0.35, $L_s = 10$ m and $\gamma = 0.6$. The wave-making internal source function is used at a distance 14.78 m from the toe of the beach. Bottom friction is not considered in this test case. The free surface elevation is recorded at gauges which are placed every 0.1 m along the center-line. The time series are analyzed evaluating the mean wave height and the position of the mean water level (MWL).

Fig. 4 illustrates the wave-by-wave treatment and the l_{NSW} area along the centerline for our hybrid model and for test case 031041, at two time instances. As they propagate shore-word, the waves gradually steepen, due to shoaling, and the surface variation criterion flags for breaking first. After a while the waves are fully broken and energy is dissipated while propagating shore-word leading to a progressive decrease of the wave breaker heights and front slopes. The surface variation criterion is active on each bore front until the fronts reach the shoreline. Individual breaking fronts can be seen as they are tracked by the model.

The numerical results of the hybrid model and the eddy viscosity one, using $\partial_t \eta^{(I)} = 0.5\sqrt{gh}$ and $\partial_t \eta^{(F)} = 0.15\sqrt{gh}$, are compared to the experimental data in Fig. 5 for case 031041. The results show the computed and measured wave heights and MWL as the wave propagates shoal and breaks up the slope. Both sets of wave breaking formulations predict reasonably well the location of the breaking event, that happens slightly earlier compared to the experimental data. This is

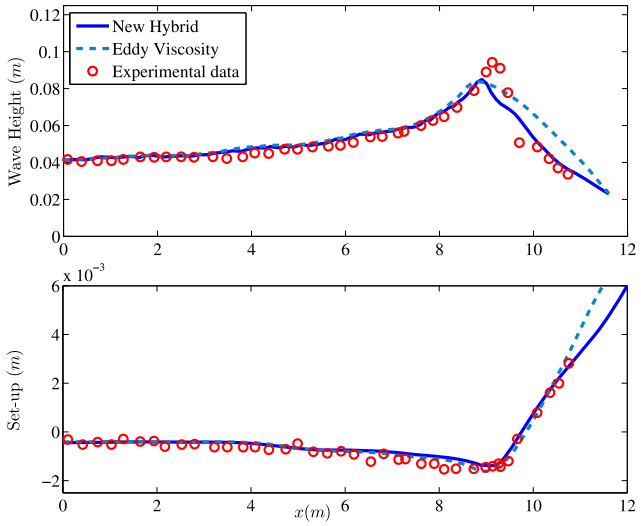

Fig. 5. Computed and measured wave heights (top) and set-up (bottom) for the Hansen and Svendsen plunging breaker 031041.

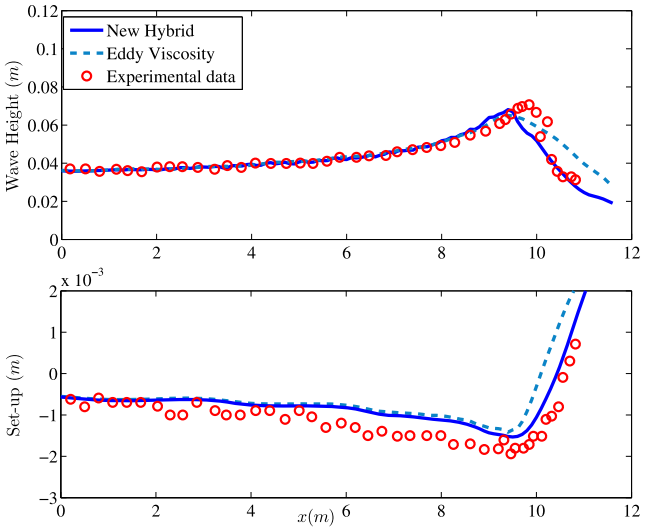

Fig. 6. Computed and measured wave heights (top) and set-up (bottom) for the Hansen and Svendsen spilling breaker 051041.

due to the overshoaling produced in the numerical wave, which is closely connected to the nature of the weakly non-linear weakly dispersive BT model used here, [37]. The differences in the wave height prediction at the swash zone, between the two models is attributed to the different nature of the wave breaking mechanisms. The hybrid mechanism represents the breaking wave as a shock storing the water spilled from the breaking wave behind the front while the eddy viscosity formulation initiates a diffusion coefficient added to the momentum equation which models the turbulent mixing and dissipation caused by breaking. Wave heights in the inner surf zone tend to be over predicted by the eddy viscosity model and this has also been observed in [37,59]. In the wave set-up results, a small discrepancy between the measured data and the numerical results can be observed and its is due to the transformation of the regular wave, as expected, since the Stokes number in this case is 17.558 and is far away of the limits of the BT equations of Nwogu.

In Fig. 6, results of the hybrid model and the eddy viscosity one are compared to the experimental data in for case 051041. Wave shoaling is again predicted moderately well for both the hybrid and the eddy viscosity model, along with a somewhat premature breaking. Again, the numerical prediction of the wave height in the inner surf zone is better for the hybrid model compared to the eddy viscosity one. The same behavior can be observed on the set-up computations.

5.3. Periodic waves breaking over a submerged bar

Beji and Battjes [6] conducted multiple laboratory experiments to examine sinusoidal wave propagation over a submerged bar. The experimental set-up was conceived to investigate the frequency dispersion characteristics and non-linear

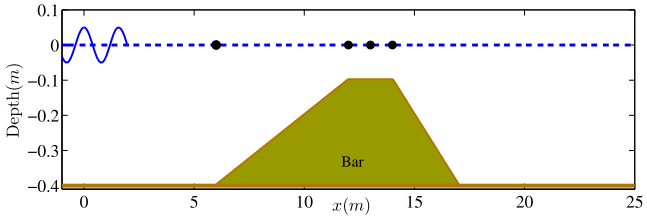

Fig. 7. Definition sketch of the numerical setup for wave breaking over a bar; black dots denote wave gauge locations.

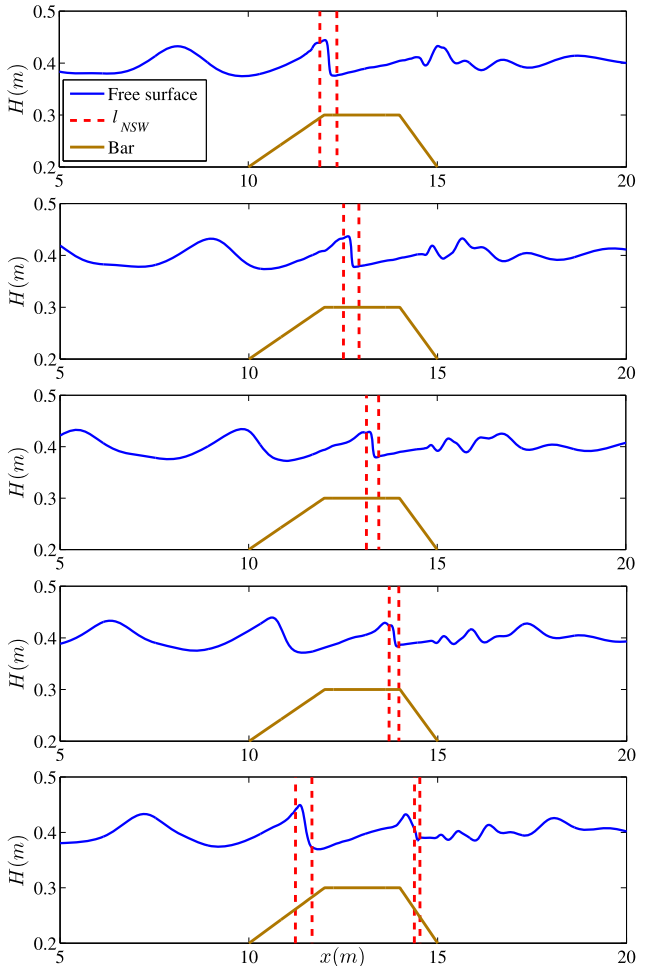

Fig. 8. Spatial snapshots along the centerline of regular waves breaking over a bar with the flow between two consecutive vertical lines governed by the NSW equations.

interaction of complex wave propagation phenomena. As the wave propagates over a submerged bar multiple transformations occur, such as non-linear shoaling, amplification of bound harmonics and wave breaking. More precisely harmonic generation occurs above the breakwater and the energy form the first harmonic is transferred to higher, phase-locked, harmonics. As the wave re-enters on deeper water (at the lee side of the bar) these higher harmonics are released as free waves. The experiments were conducted in a 37.7 m long, 0.8 m wide, and 0.75 m high wave flume. A hydraulically driven, piston-type random wave generator was located at the left side of the flume and a 1 : 25 plane beach with coarse material was placed at the right side to serve as a wave absorber. The submerged trapezoidal bar was 0.3 m high with front slope of 1 : 20 and lee slope of 1 : 10 separated by a level plateau 2 m in length.

We consider here the test case with wave height 0.054 m and $T = 2.5$ s wave period that corresponds to the water depth parameter $kh \approx 0.52$, with depth to wavelength ratio of $h/L = 0.0835$. The wave-making internal source function at $x = 0$ m. The dimensions of the computational domain were set to $(x, y) \in [-26, 26\text{ m}] \times [0, 0.8\text{ m}]$ with sponge layer widths is set to $L_s = 10$ m at both ends of the computational domain. For the computation a triangular grid was used, consisting

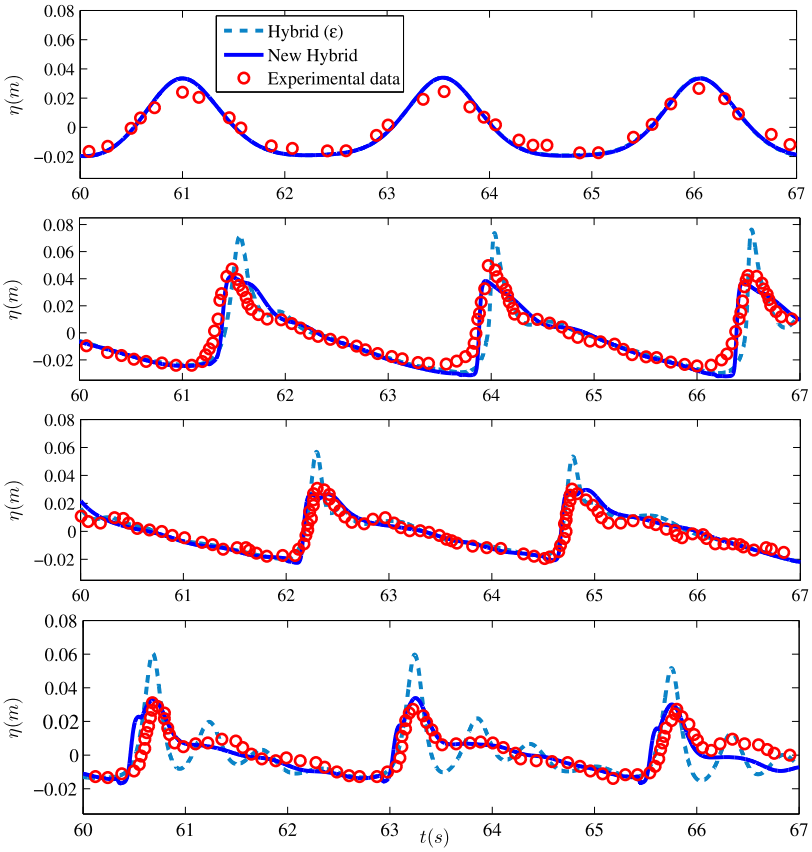

Fig. 9. Time series of surface elevation at wave gauges for periodic wave breaking over a bar.

of equilateral triangles with side length of $h_N = 0.014$ m, leading to a mesh of $N = 25{,}078$ nodes. The CFL number used was set equal to 0.35 with the value of γ now set to 0.3 following the discussion in Section 4.2.1. Since we are interested only on the breaking behavior of the model and due to the inability of the BT model to fully resolve the higher harmonics released at the lee side of the bar [36], only four wave gauges were placed at $x = 6, 12, 13$ and 14 m respectively as shown in Fig. 7, along with the problem's geometry along the centerline.

In the wave evolution, waves shoal along the front slope, since non-linear effects cause the waves propagating along this slope to steepen and broke at the beginning of the bar crest. Breaking is classified as plunging. In the lee side, the back slope causes the wave train to breakup into independent waves traveling at their own speed. Hence, bound higher harmonics are developed along the front slope, which are then released from the carrier frequency on the lee side of the bar as the water depth parameter kh increases rapidly. Fig. 8 illustrates the wave-by-wave treatment and the l_{NSW} area along the centerline for our hybrid model at different time instances (covering roughly one wave period). The onset of breaking is correctly predicted close to the beginning of the bar crest and continues along the flat of the bar leading to a wave height decay. Individual breaking fronts can be seen again as they are tracked by the model.

Fig. 9 shows the computed and recorded wave forms at the four wave gauges of interest. The numerical results of the new hybrid model are compared with those produce by the Hybrid(ϵ) model and the experimental ones. The wave shape is well-reproduced by the new hybrid model for all wave gauges. The wave height decay on the top of the bar compare very well with the experimental data. The results obtained with the Hybrid(ϵ) model, although they are in phase with the experimental data, overestimate the predicted wave height resulting in a different wave shape at the last gauge. These results are due to the inability of this model to dissipate correctly the wave energy of the broken waves on the top of the bar, since wave breaking ceases before all the wave energy is dissipated as discussed in Section 4. One way to overcome this problem would have been to pre-specify the region on the bar top to be governed by the NSW model but this cannot be consider as a universal approach in the application of this model.

5.4. Solitary wave propagation over a two-dimensional reef

The next experimental test case initially presented in [56] is on solitary wave transformations over an idealized fringing reef and examines the model's capability in handling non-linear dispersive waves along with wave breaking and bore propagation. The laboratory experiments carried out at the O.H. Hinsdale Wave Research Laboratory of Oregon state University

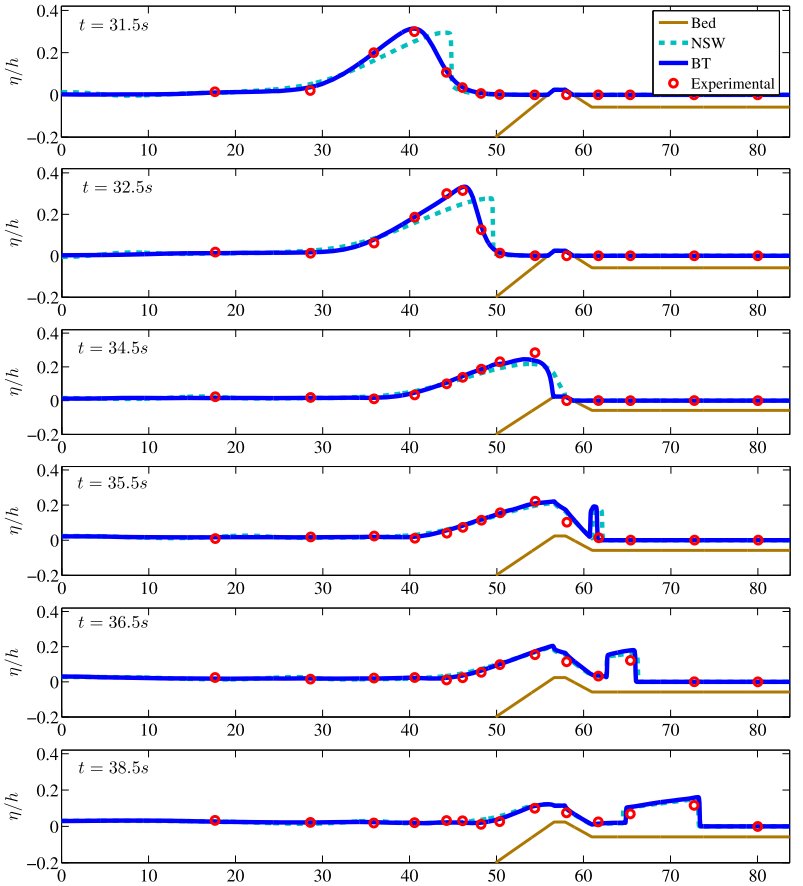

Fig. 10. Evolution of surface profiles and wave transformations over an exposed reef for $A/h = 0.3$ and 1/12 slope.

from 2007–2009. The test presented here include a steep slope along with a reef crest in order to represent fringing reefs, found in tropical environments. The computational domain is $(x, y) \in [0, 83.7\ \text{m}] \times [0, 1.1\ \text{m}]$ and the topography includes a fore reef slope of 1/12 a 0.2 m reef crest and a water depth $h = 2.5$ m. The reef crest is then exposed by 6 cm and submerges the flat with $h = 0.14$ m. This test case involves a 0.75 m high solitary wave which gives a dimensionless wave high of $A/h = 0.3$. The computational mesh used has $h_N = 0.05$ leading to $N = 43{,}563$ mesh nodes. A CFL number of 0.35 was used, the wet/dry threshold parameter $\epsilon_{wd} = 1.d - 6$ and $\gamma = 0.6$. Wall boundary conditions were placed at each boundary of the computational domain and as suggested in [55] a Manning coefficient $n_m = 0.014\ \text{s/m}^{1/3}$ was used, to define the roughness of the concrete surface of the reef. Experimental results for the free surface elevation were recorded at 14 wave gauges [56] along the centerline of the computational domain.

Figs. 10 and 11 compare the measured and computed wave profiles as the numerical solitary wave propagates. The numerical solutions of the new hybrid BT model is compared also with that of the NSW equations. As the initially symmetric solitary wave shoals across the toe of the slope at $x = 25.9$ m, it begins to skew to the front with the NSW equations forming a vertically-faced propagating bore. Experimentally the wave begins to break around $t = 33$ s developing a plunging breaker on the top of the reef crest that collapsed around $t = 34.5$ s. Both models are mimicking the breaker as a collapsing bore that slightly underestimates the wave height but conserved the total mass. By time $t = 35.5$ s the broken wave begins to travel down the back slope of the reef crest generating a supercritical flow that displaces the initially stagnant water, generating a hydraulic jump off the back reef and a downstream propagating bore fueled by the supercritical flow mass and momentum transfer. Laboratory observations indicated this generation of the hydraulic jump and an overturning of the free surface off the back reef along with a turbulent bore propagating downstream. Around $t = 40$ s the momentum flux balances at the flow discontinuity and the hydraulic jump becomes stationary momentarily, while the bore continues to propagate downstream. The hybrid model predicts correctly the phase and amplitude of the discontinuities indicating the correct energy dissipation during wave breaking.

At subsequent times, the end wall reflects a bore back that by time $t = 54$ s has over-toped the reef crest generating a hydraulic jump on the fore reef and a reflected bore at the back of the reef that travels again downstream. At this point, and as the water rushes down the fore reef, the flow transitions from flux to dispersion-dominated through the hydraulic jump. The hydraulic jump generates an offshore propagating undular bore, which transforms into a train of dispersive waves

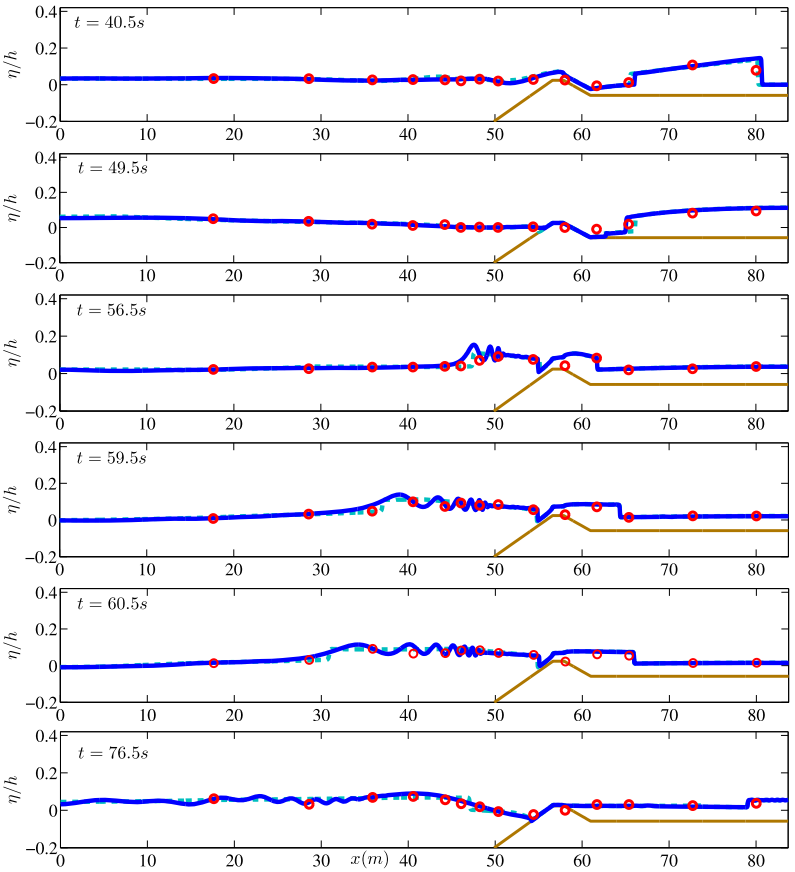

Fig. 11. Evolution of surface profiles and wave transformations over an exposed reef for $A/h = 0.3$ and 1/12 slope.

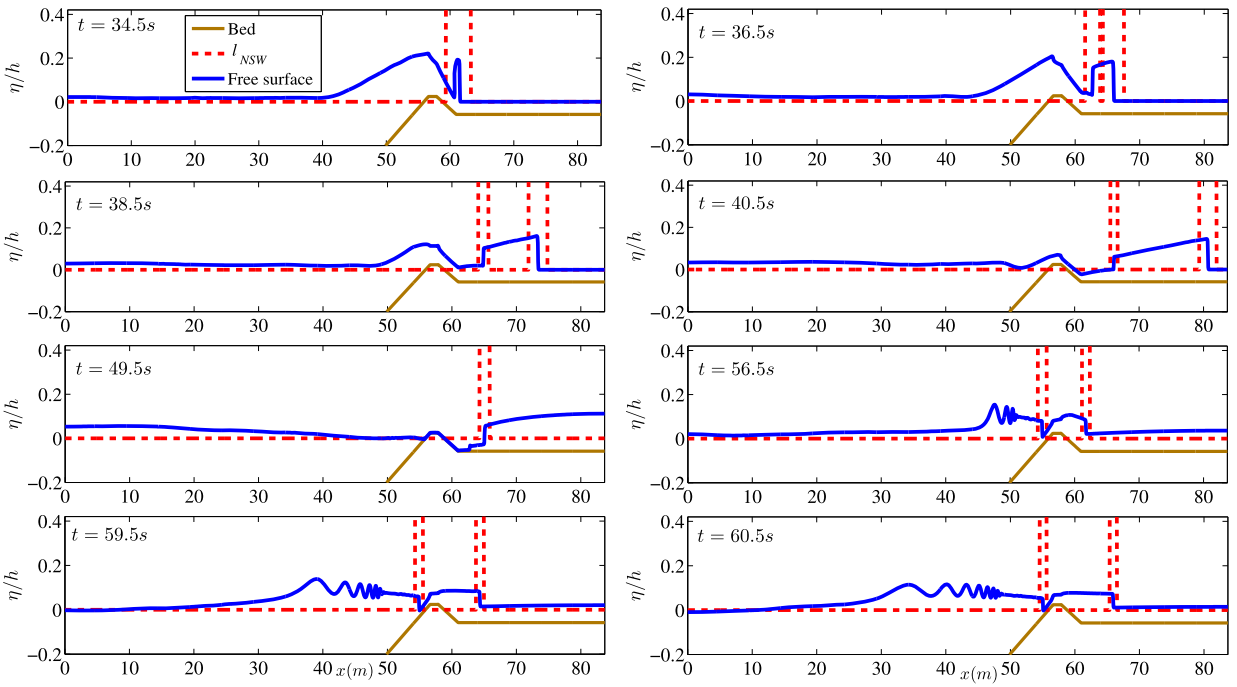

Fig. 12. Spatial snapshots along the centerline of a solitary wave propagation over a two-dimensional reef with the flow between two consecutive vertical lines governed by the NSW equations.

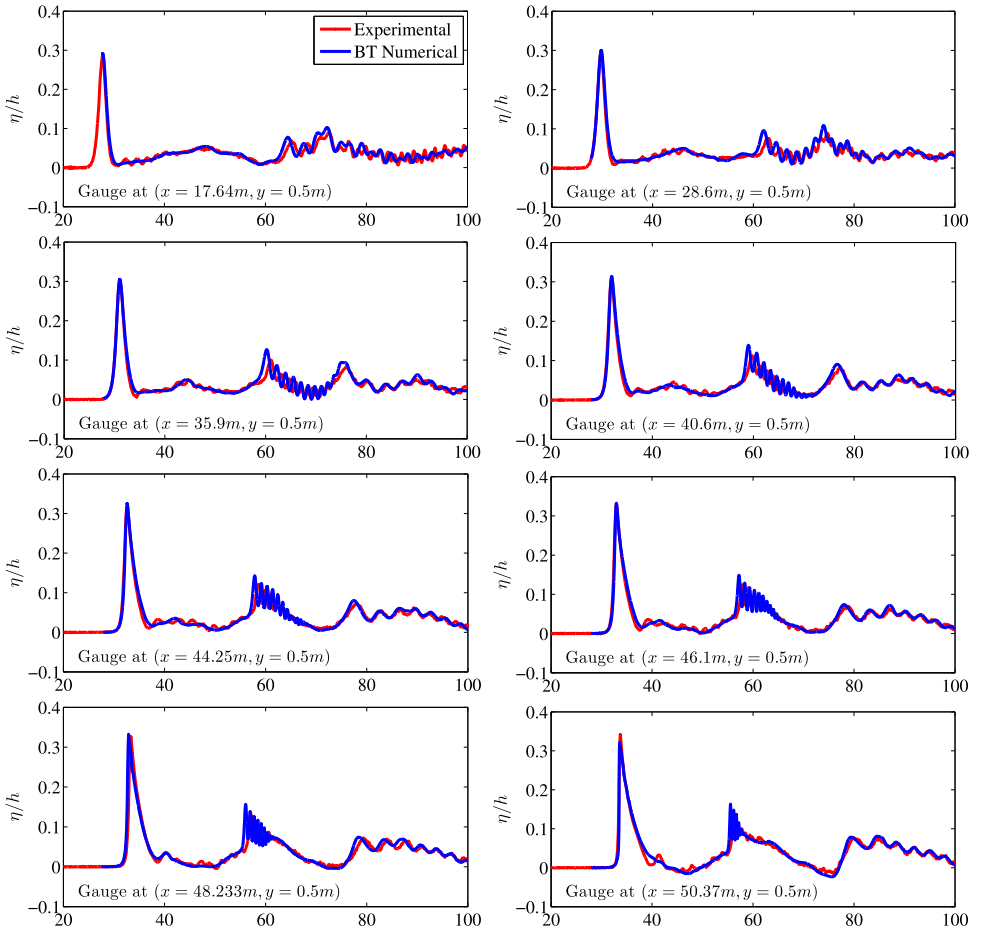

Fig. 13. Time series of the normalized free surface at the wave gauges before the reef.

over the increasing water depth. The created bore at the fore reef propagates as a shock for the NSW equations offshore due to the hyperbolic character of the equations, as can be seen in Fig. 11. The NSW model totally smooths the results with an additional phase shift. On the other hand, the BT model reproduces correctly the decaying undular bore as well as the subsequent higher harmonics released at later times.

The use of the proposed breaking criteria is critical, in this particularly challenging test case, in order to capture the stationary and nearly stationary jumps and reflected bores on the flow profile. The evolution of the breaking regions can be seen in Fig. 12. Stationary hydraulic jumps are correctly recognized by the local slope angle criterion in all instances. The development of an undular bore in the flow justifies the use of the critical Froude termination criterion which correctly recognizes the non-breaking undular bore which is resolved by the BT model as it travels in deeper waters.

Figs. 13 and 14 compare the computed and recorded surface elevation time series at specific wave gauges. Fig. 13 compares the computed and recorded surface elevation time series at the wave gauges before the reef and Fig. 14 after the reef. The recorded data from the wave gauges at $x \leqslant 50.4$ m shows the effect of the dispersive waves on the free surface. The produced train of waves over the increasing water depth and the resulting undulations were intensified as higher harmonics were released. As a matter of fact, wave gauges near the toe of the slope recorded highly dispersive waves of $kd > 30$ [56]. The hybrid BT model managed to reproduce these highly dispersive waves with the correct phase and height strengths. The time series at $x = 58.1$ m present the initial and subsequently over-toppings at the reef crest and confirm the efficiency of the applied wet/dry front treatment. The numerical model reproduced these over-toppings at the correct phase but slightly overestimated the height of the arrival waves. At the gauges located at $x = 65.38$ m, 72.7 m and 80 m, the arrival of the initial wave, the first reflected bore from the end wall, its subsequent reflection from the back reef as well as any subsequent reflections are almost correctly reproduced by the numerical model.

5.5. Solitary wave propagation over a three-dimensional reef

Swingler and Lynett [67] performed laboratory experiments in the O.H. Hinsdale Wave Research Laboratory of Oregon State University, to study specific phenomena, that are known to occur when solitary waves approach a shoreline, such as

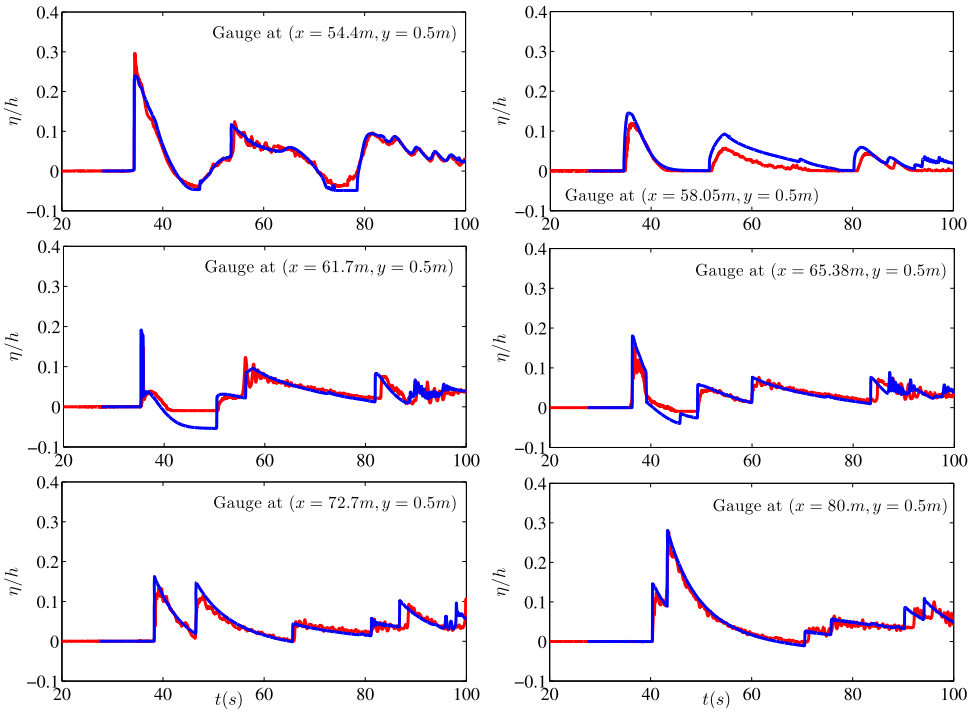

Fig. 14. Time series of the normalized free surface at the wave gauges on top and after the reef.

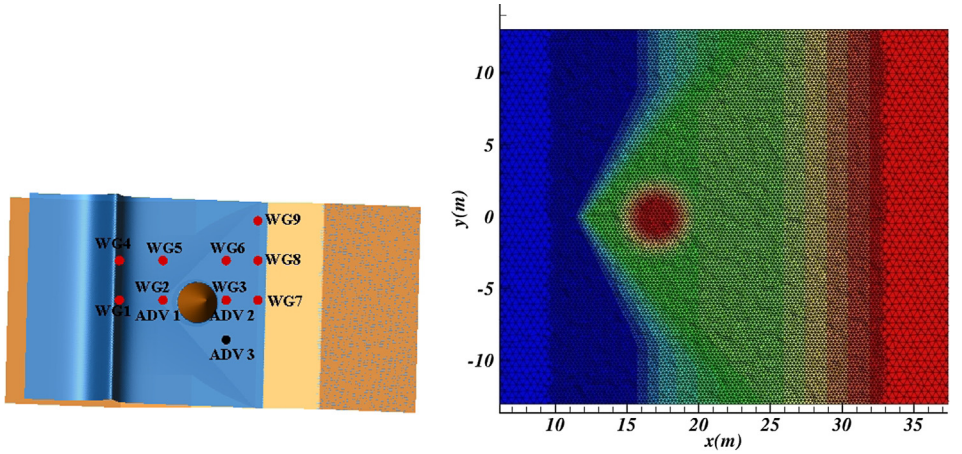

Fig. 15. Three-dimensional reef problem geometry: wave gauges's, ADVs's locations (left) and close-up of the unstructured grid (right).

shoaling, refraction, breaking and turbulence inducing complex dynamics for model validation [55,59]. The basin is 48.8 m long 26.5 m wide and 2.1 m deep. A complex bathymetry from $x = 10.2$ m to $x = 2.5$ m consisting of a 1 : 30 is connected with a triangular reef flat submerged between 7.5 cm and 9 cm below the still water level. The offshore shelf edge has an elevation of 0.71 m with the apex located at $x = 12.6$ m. The steepest slope of the shelf is at the apex and becomes milder moving along the shelf edge toward the basin side walls. The planar beach continues to $x = 31$ m and then becomes level until the back of the basin. In addition, a concrete cone of 6 m diameter and 0.45 m height was placed to the apex of the reef between $x = 14$ m and $x = 20$ m.

Nine wave gauges where placed to measure the free surface elevation along with three Acoustic Doppler Velocimeters (ADVs) alongshore and cross-shore to measure the velocity as shown in Fig. 15. Gauges $1, 2, 3, 7$ where located at $y = 0$ m and at $x = 7.5, 13.0, 21.0, 25$ m respectively, while gauges $4, 5, 6, 8$ where located at $y = 5$ m and $x = 7.5, 13, 21, 25$ m. ADVs 1–3 are placed at $(13.0, 0.0)$ m, $(21.0, 0.0)$ and $(21.0, -5.0)$ m respectively.

The computational domain is extended from $x = 0$ m to $x = -5$ m with a constant water depth of 0.78 m. An unstructured mesh, refined along the shelf (using the h-enrichment technique from [47]), with $N = 87,961$ nodes has been created for this problem, with $h_N = 0.1$ m at the refined region. Wall boundary conditions were imposed at the boundaries, the CFL

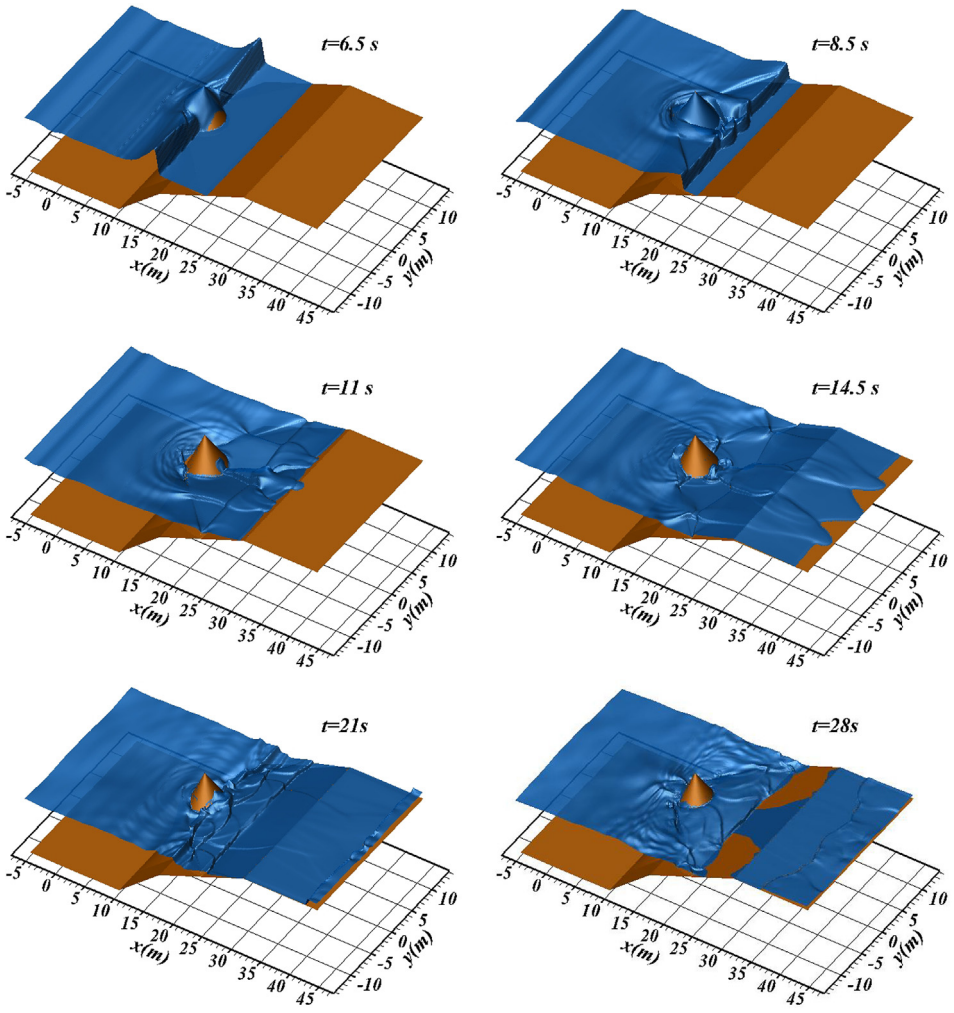

Fig. 16. Water surface for solitary wave propagation on a 3D reef at different times.

value used was 0.4 and $\gamma = 0.6$. A solitary wave of 0.39 m in height is placed along $x = 5$ m at time $t = 0$ s. It should be mentioned that, $A/h = 0.5$ in this problem which constitutes a particular demanding case for the BT model used due to its high non-linearity.

Fig. 16 shows the computed water surfaces at various times. At the initial stages the wave front becomes very steep as the solitary wave advances on the self. The solitary wave begins to break along the centerline around $t = 5$ s, when it crosses the shelf's apex. By time $t = 6.5$ s the resulting surge completely overtops the cone while the wave along the basin's sides continuous to shoal. By time $t = 8.5$ s the refracted waves and the diffracted waves collide on the shelf. The refracted waves collide at the lee side of the cone as edge waves which propagate around the two sides of the cone. Around $t = 11$ s the water withdraws from the cone and the bore-front from the diffracted wave propagates onshore and reinforces the refracted waves from the reef edge. At subsequent times the water advances up the slope and reaches the flat area. Around $t = 14.5$ s a new bore is created, from the draw-down of the water on the slope, and collides with the refracted waves while water propagates on the flat area. By time $t = 21$ s part of the diffracted and refracted waves are trapped around the cone while water continuous to draw-down the slope which by $t = 28$ s becomes almost dry.

Fig. 17 shows the time series of the computed surface elevation recorded measurements at WG 1–9. At the first two gauges the arrival of the wave is almost correctly predicted. WG 2 is located at the point where wave breaking is initiated. The collision of the refracted and diffracted waves at the lee side of the cone is almost exactly computed by the model without an over-prediction of the wave height as can be seen from the results in WG 3 around time $t = 8$ s. The data and model comparisons at WGs 4, 5, 6, 8 and 9, located at the north side of the shelf, indicate that the numerical model predicts wave shoaling, refraction and breaking on the shelf reasonably well. The onshore propagation of the diffracted waves and the subsequent water recession is well predicted as indicated by the results at WG 7. We note here that, after time $t = 40$ s the numerical results start to deviate from the measurements due to late arrival of the numerical reflected waves from the extended computational domain.

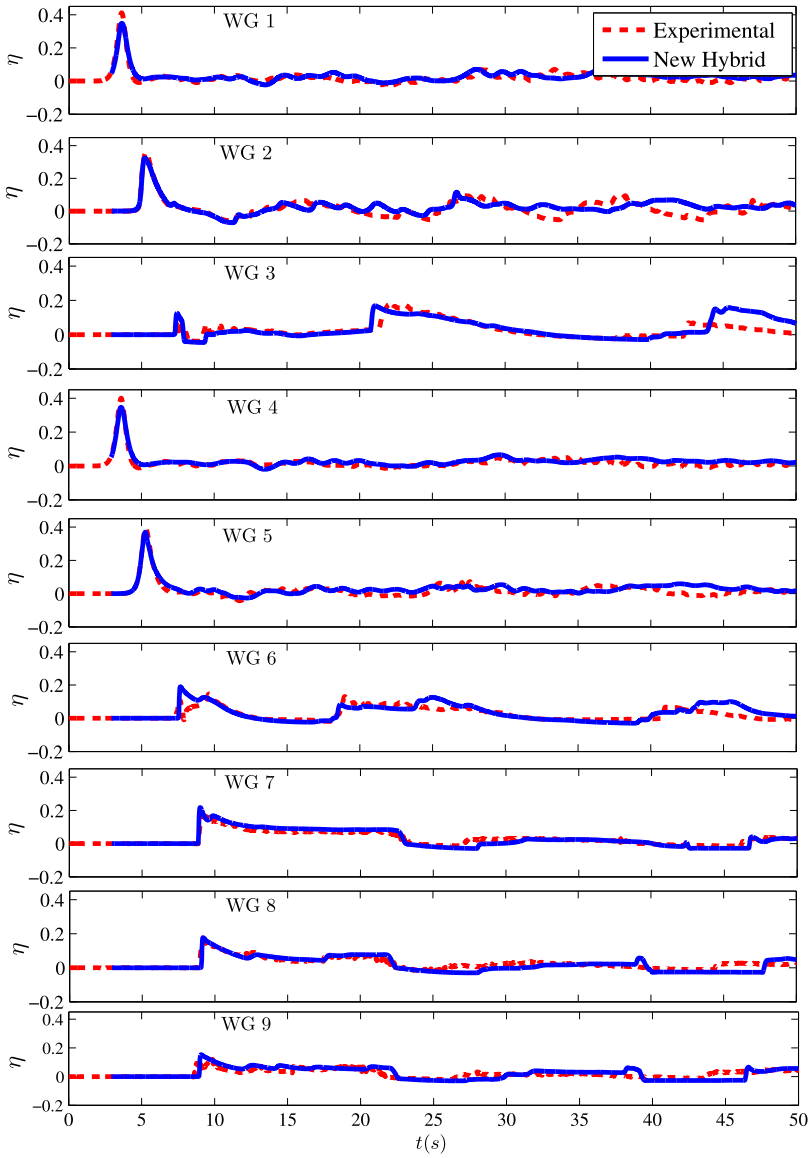

Fig. 17. Time series of surface elevation for solitary wave propagation on a 3D reef.

Finally, in Fig. 18 the velocity time series measurements are compared with the numerical ones at the different ADVs locations. The hybrid BT model matches the u-components of the velocity reasonably well by predicting correctly peak velocities as well as the entire trend in time of the u-velocity profiles. The v-velocity results were not compared with measurements from ADV 1 and ADV 2 since the measurement values were too small, a similar observation was made in [59]. The production of the v-component of the velocity is well predicted by the numerical model at the location of ADV 3. It is noted that, the measurements at ADV 3 record the initial wave's shoaling, breaking and refraction.

6. Concluding remarks

In this paper, a new approach to handle wave breaking for an unstructured finite volume scheme solving the extended BT equations of Nwogu has been presented. This new approach is of the hybrid-type meaning that the strategy proposed is that of switching to NSW equations, by locally suppressing the dispersion terms, in the vicinity of a breaking wave. In this way broken wave fronts are treated as shocks by the NSW equations and the conservative and shock capturing properties of the numerical scheme are exploited. A certain combination of criteria is established to characterize the initiation of breaking based on the free surface variation and the local slope angle, with only a few parameters needing to be calibrated depending on the test case. More precisely, in the test cases considered in this work, only the parameter that governs the surface variation criterion had to be adjusted and only for the case of regular waves propagating over a submerged bar.

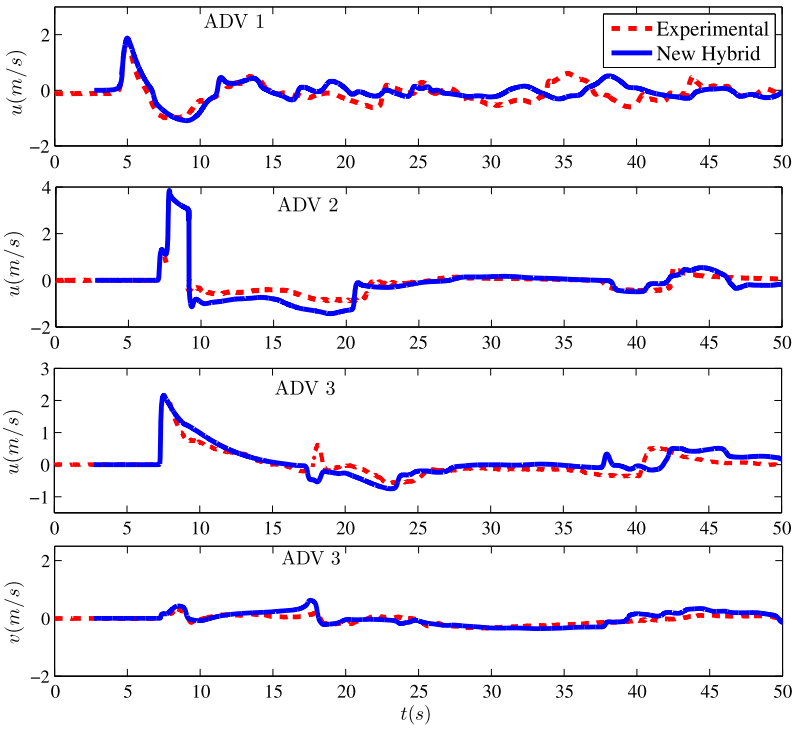

Fig. 18. Time series of velocity components at the different ADVs for solitary wave propagation on a 3D reef.

The complementary nature of these two criteria was proven efficient and robust in tracking broken wave fronts as well as stationary breaking or partially breaking hydraulic jumps. An additional termination criterion is also considered which is based on the wave's Froude number, particularly suited for the characterization of undular bores. In addition, a stable methodology is developed for the smooth transition between the two models (BT/NSW), within our FV framework, when wave breaking occurs in a numerical simulation. With this methodology, any non-physical mix of the two models is avoided and there is no need for any numerical filtering to be applied.

Our proposed model has been extensively validated against experimental data from various benchmark problems. The model was able to intrinsically capture the location and evolution of breaking events, in all the test cases considered, and provided improved results compared to other wave breaking treatments. The model has been proven efficient and robust, within the applicability limits of the governing equations which have weakly non-linear and dispersive properties. However, we consider the proposed wave breaking treatment presented as quite general and we conjecture that can be adapted to numerical approximations of fully non-linear BT models which may follow from this work.

Appendix A

The 2×2 matrices in (19) are constructed as:

$$\mathbf{A}_Q = \frac{1}{2|M_{PQ}|}\begin{bmatrix} \sum_{R,Q\in K_P\cap K_{PQ}}(n_{PRx}+n_{RQx})n_{PQ_x} & \sum_{R,Q\in K_P\cap K_{PQ}}(n_{PRy}+n_{RQy})n_{PQ_x} \\ \sum_{R,Q\in K_P\cap K_{PQ}}(n_{PRx}+n_{RQx})n_{PQ_y} & \sum_{R,Q\in K_P\cap K_{PQ}}(n_{PRy}+n_{RQy})n_{PQ_y} \end{bmatrix},$$

$$\mathbf{B}_Q = \frac{1}{2|M_{PQ}|}\begin{bmatrix} \sum_{R,Q\in K_P\cap K_{PQ}}h_R(n_{PRx}+n_{RQx})n_{PQ_x} & \sum_{R,Q\in K_P\cap K_{PQ}}h_R(n_{PRy}+n_{RQy})n_{PQ_x} \\ \sum_{R,Q\in K_P\cap K_{PQ}}h_R(n_{PRx}+n_{RQx})n_{PQ_y} & \sum_{R,Q\in K_P\cap K_{PQ}}h_R(n_{PRy}+n_{RQy})n_{PQ_y} \end{bmatrix},$$

$$\mathbf{A}_P = \frac{1}{2|M_{PQ}|}\begin{bmatrix} (n_{SPx}+n_{PRx})n_{PQ_x} & (n_{SPy}+n_{PRy})n_{PQ_x} \\ (n_{SPx}+n_{PRx})n_{PQ_y} & (n_{SPy}+n_{PRy})n_{PQ_y} \end{bmatrix} \quad \text{and} \quad \mathbf{B}_P = h_P\mathbf{A_P}.$$

The number of geometrical entries in each summation is always two, while the number of entries in the summation $\sum_{Q\in K_P}$ in (19) is equal to the number of the neighbors of P. This means that the maximum non-zero elements of the matrix $\mathbf{M}$ in each row P in (19) are two times the number of the neighbors of P plus one.

References

[1] T.J. Barth, A 3-D upwind Euler solver for unstructured meshes, AIAA paper 91-1548CP.

[2] T.J. Barth, Aspects of unstructured grids and finite volume solvers for the Euler and Navier–Stokes equations, in: Special Course on Unstructured Grid Methods for advection Dominated Flows, 1992, AGARD Report 787.
[3] T.J. Barth, Numerical Methods and Error Estimation for Conservation laws on Structured and Unstructured Meshes, VKI Computational Fluid Dynamics Lecture Series, 2003.
[4] T.J. Barth, M. Ohlberger, Finite volume methods: foundation and analysis, in: E. Stein, R. de Borst, T. Hudges (Eds.), Encyclopedia of Computational Mechanics, John Wiley and Sons Ltd., 2004.
[5] D.R. Basco, I.A. Svendsen, Modeling turbulent bore propagation in the surf zone, in: Proceeding of the 19th International Conference on Coastal Engineering, 1984.
[6] S. Beji, J.A. Battjes, Experimental investigations of wave propagation over a bar, Coast. Eng. 19 (1993) 151.
[7] A. Bermudez, A. Dervieux, J.A. Desideri, M.E. Vázquez, Upwind schemes for the two-dimensional shallow water equations with variable depth using unstructured meshes, Comput. Methods Appl. Mech. Eng. 155 (1–2) (1998) 49.
[8] H.B. Bingham, P.A. Madsen, D.R. Fuhraman, Velocity potential formulations of highly accurate Boussinesq-type models, Coast. Eng. 56 (2009) 467.
[9] P. Bonneton, E. Barthelemy, F. Chazel, R. Cienfuegos, D. Lannes, F. Marche, M. Tissier, Resent advances in Serre–Green Naghdi modelling for wave transformation breaking and runup processes, Eur. J. Mech. B, Fluids 30 (2011) 589–597.
[10] P. Bonneton, F. Chazel, D. Lannes, F. Marche, M. Tissier, A splitting approach for the fully nonlinear and weakly dispersive Green–Naghdi model, J. Comput. Phys. 230 (2011) 1479–1498.
[11] A.G.L. Borthwick, M. Ford, B.P. Weston, P.H. Taylor, P.K. Stansby, Solitary wave transformation, breaking and run-up at a beach, Marit. Eng. 159 (2006) 97–105.
[12] J. Boussinesq, Théorie des ondes et des remous qui se propagent le long d'un canal rectangulaire horizontal, en communiquant au liquide contenu dans ce canal des vitesses sensiblement pareilles de la surface au fond, J. Math. Pures Appl. 17 (1872) 55–108.
[13] M. Brocchini, A reasoned overview on Boussinesq-type models: the interplay between physics, mathematics and numerics, Proc. R. Soc. A 469 (2013), http://dx.doi.org/10.1098/rspa.2013.0496.
[14] P. Brufau, P. García-Navarro, M.E. Vázquez-Cendón, Zero mass error using unsteady wetting–drying conditions in shallow flows over dry irregular topography, Int. J. Numer. Methods Fluids 45 (2004) 1047–1082.
[15] P. Brufau, M.E. Vázquez-Cendón, P. Gracía-Navarro, A numerical model for the flooding and drying of irregular domain, Int. J. Numer. Methods Fluids 39 (2002) 247.
[16] M.J. Castro, A.M. Ferreiro, J.A. García-Rodriguez, J.M. González-Vida, J. Macías, C. Parés, M.E. Vázquez-Cendón, The numerical treatment of wet/dry fronts in shallow flows: Application to one-layer and two-layer systems, Math. Comput. Model. 42 (2005) 419–439.
[17] R. Cienfuegos, E. Barthélemy, P. Bonneton, A fourth-order compact finite volume scheme for fully nonlinear and weakly dispersive Boussinesq-type equations. Part I: Model development and analysis, Int. J. Numer. Methods Fluids 51 (2006) 1217–1253.
[18] R. Cienfuegos, E. Barthélemy, P. Bonneton, A fourth-order compact finite volume scheme for fully nonlinear and weakly dispersive Boussinesq-type equations. Part II: Boundary conditions and validation, Int. J. Numer. Methods Fluids 53 (2007) 1423–1455.
[19] R. Cienfuegos, E. Barthélemy, P. Bonneton, Wave-breaking model for Boussinesq-type equations including roller effects in the mass conservation equation, J. Waterw. Port Coast. Ocean Eng. 136 (2010) 10–26.
[20] F. D'Alessanro, G. Tomasicchio, The BCI criterion for the initiation of breaking process in Boussinesq-type equations wave models, Coast. Eng. 55 (2008) 1174–1184.
[21] A.I. Delis, M. Kazolea, Finite volume simulations of waves formed by sliding masses, Commun. Numer. Methods Eng. 27 (2011) 732–757.
[22] A.I. Delis, M. Kazolea, N.A. Kampanis, A robust high resolution finite volume scheme for the simulation of long waves over complex domain, Int. J. Numer. Methods Fluids 56 (2008) 419–452.
[23] A.I. Delis, I.K. Nikolos, M. Kazolea, Performance and comparison of cell-centered and node-centered unstructured finite volume discretizations for shallow water free surface flows, Arch. Comput. Methods Eng. 18 (2011) 57–118.
[24] W. El Asmar, O. Nwogu, Finite volume solution of Boussinesq-type equations on an unstructured grid, in: J. McKee Smith (Ed.), Proceedings of the 30th International Conference on Coastal Engineering, San Diego, CA, USA, 2006.
[25] K.S. Erduran, V. Kutija, C.J.M. Hewett, Performance of finite volume solutions to the shallow water equations with shock-capturing schemes, Int. J. Numer. Methods Fluids 40 (2002) 1237.
[26] D.R. Fuhrman, P.A. Madsen, Simulation of nonlinear wave run-up with a high-order Boussinesq model, Coast. Eng. 55 (2008) 139–154.
[27] A. George, J.W.H. Liu, Computer Solution of Large Sparse Positive Definite Systems, Prentice Hall, Englewood Cliffs, N.J., 1981.
[28] M.F. Gobbi, J.T. Kirby, G. Wei, A fully non-linear Boussinesq model for surface waves. Part 2. Extension to o(kh4), J. Fluid Mech. 405 (2000) 181.
[29] E. Godlewski, P.A. Raviart, Hyperbolic Systems of Conservation Laws, Applied Mathematical Sciences, vol. 118, Springer, Berlin, 1995.
[30] J.B. Hansen, I.A. Svendsen, Regular waves in shoalling water: experimental data, Technical Report, ISVA Series Paper, vol. 21, 1979.
[31] K.L. Heithner, G.W. Housner, Numerical model for tsunami runup, J. Waterw. Port Coast. Ocean Eng. 96 (1970) 701–719.
[32] M.E. Hubbard, P. García-Navarro, Flux difference splitting and the balancing of source terms and flux gradients, J. Comput. Phys. 165 (2000) 89–125.
[33] T.V. Karambas, Nonlinear wave energy modeling in the surf zone, Nonlinear Process. Geophys. 3 (1996) 127–134.
[34] T.V. Karambas, C. Koutitas, A breaking wave propagation model based on the Boussinesq equations, Coast. Eng. 18 (1992) 1–19.
[35] M. Kazolea, A.I. Delis, A well-balanced shock-capturing hybrid finite volume-finite difference numerical scheme for extended 1D Boussinesq models, Appl. Numer. Math. 67 (2013) 167–186.
[36] M. Kazolea, A.I. Delis, I.K. Nikolos, C.E. Synolakis, An unstructured finite volume numerical scheme for extended 2D Boussinesq-type equations, Coast. Eng. 69 (2012) 42–66.
[37] A.B. Kennedy, Q. Chen, J.T. Kirby, R.A. Dalrymple, Boussinesq modeling of wave transformation, breaking and runup. Part I: 1D, J. Waterw. Port Coast. Ocean Eng. 126 (2000) 39–47.
[38] D.-H. Kim, P.J. Lynett, S.A. Socolofsky, A depth-integrated model for weakly dispersive, turbulent, and rotational fluid flows, Ocean Model. 27 (2009) 198–214.
[39] Q. Liang, A.G.L. Borthwick, Adaptive quadtree simulation of shallow flows with wet-dry fronts over complex topography, Comput. Fluids 38 (2009) 221–234.
[40] P. Lynett, P.L.F. Liu, A two-layer approach to wave modeling, Proc. R. Soc. Lond. Ser. A 460 (2004) 2637.
[41] P.J. Lynett, Nearshore wave modeling with high-order Boussinesq-type equations, J. Waterw. Port Coast. Ocean Eng. 132 (2006) 348–357.
[42] P.J. Lynett, T.R. Wu, P.L.F. Liu, Modeling wave runup with depth integrated equations, Coast. Eng. 46 (2002) 98–107.
[43] P. Madsen, O.R. Sørensen, H.A. Schäffer, Surf zone dynamics simulated by a Boussinesq-type model: Part I. Model description and cross-shore motion of regular waves, Coast. Eng. 32 (1997) 255–288.
[44] P. Madsen, O.R. Sørensen, H.A. Schäffer, Surf zone dynamics simulated by a Boussinesq-type model: Part II. Surf beat and swash oscillations for wave groups and irregular waves, Coast. Eng. 32 (1997) 289–319.
[45] P.A. Madsen, H.A. Schäffer, Higher-order Boussinesq-type equations for surface gravity waves: derivation and analysis, Philos. Trans. R. Soc. Lond. 356 (1998) 3123–3184.
[46] P.A. Madsen, O.R. Sørensen, A new form of the Boussinesq equations with improved linear dispersion characteristics. Part 2: A slowing varying bathymetry, Coast. Eng. 18 (1992) 183–204.

[47] I.K. Nikolos, A.I. Delis, An unstructured node-centered finite volume scheme for shallow water flows with wet/dry fronts over complex topography, Comput. Methods Appl. Mech. Eng. 198 (2009) 3723–3750.
[48] O. Nwogu, An alternative form of the Boussinesq equations for nearshore wave propagation, J. Waterw. Port Coast. Ocean Eng. 119 (1994) 618–638.
[49] T. Okamoto, D.R. Basco, The relative trough Froude number for initiation of wave breaking: Theory, experiments and numerical model confirmation, Coast. Eng. 53 (2006) 675–690.
[50] J. Orszaghova, A.G.L. Borthwick, P.H. Taylor, From the paddle to the beach – A Boussinesq shallow water numerical wave tank based on Madsen, and Sørensen's equations, J. Comput. Phys. 231 (2012) 328–344.
[51] D.H. Peregrine, Long waves on a beach, J. Fluid Mech. 27 (1967) 815–882.
[52] D.H. Peregrine, I.A. Svendsen, Spilling breaker, bores and hydraulic jumps, in: Proceeding of the 16th International Conference on Coastal Engineering, 1978.
[53] M. Ricchiuto, A. Bollermann, Stabilized residual distribution for shallow water simulations, J. Comput. Phys. 1071 (2009) 1115.
[54] P.L. Roe, Approximate Riemann solvers, parameter vectors, and difference schemes, J. Comput. Phys. 43 (1981) 357–372.
[55] V. Roeber, K. Cheung, Boussinesq-type model for energetic breaking waves in fringing reef environment, Coast. Eng. 70 (2012) 1–20.
[56] V. Roeber, K.F. Cheung, M.H. Kobayashi, Shock-capturing Boussinesq-type model for nearshore wave processes, Coast. Eng. 57 (2010) 407–423.
[57] Y. Saad, Iterative Methods for Sparse Linear Systems, PWS, 1996.
[58] H.A. Schäffer, P. Madsen, R. Deigaard, A Boussinesq model for waves breaking in shallow water, Coast. Eng. 20 (1993) 185–202.
[59] F. Shi, J.T. Kirby, J.C. Harris, J.D. Geiman, S.T. Grilli, A high-order adaptive time-stepping tvd solver for Boussinesq modeling of breaking waves and coastal inundation, Ocean Model. 43–44 (2012) 36–51.
[60] J.B. Shiach, C.G. Mingham, A temporally second-order accurate Godunov-type scheme for solving the extended Boussinesq equations, Coast. Eng. 56 (2009) 32–45.
[61] P. Smit, M. Zijlema, G. Stelling, Depth-induced wave breaking in a non-hydrostatic, near-shore wave model, Coast. Eng. 76 (2013) 1–16.
[62] T.M. Smith, M.F. Barone, R.B. Bond, Comparison of reconstruction techniques for unstructured mesh vertex centered finite volume schemes, in: 18th AIAA Computational Fluid Dynamics Conference, 2007, pp. 1–22.
[63] S. Soares-Frazão, V. Guinot, A second order semi-implicit hybrid scheme for one-dimensional Boussinesq-type waves in rectangular channels, Int. J. Numer. Methods Fluids 58 (2008) 237–261.
[64] O.R. Sørensen, H.A. Schäffer, P.A. Madsen, Surf zone dynamics simulated by a Boussinesq type model: Part III. Wave-induced horizontal nearshore circulations, Coast. Eng. 33 (1998) 155–176.
[65] R.J. Spiteri, S.J. Ruuth, A new class of optimal high-order strong-stability-preserving time discretization methods, SIAM J. Numer. Anal. 40 (2002) 469.
[66] I. Svendsen, Mass flux and undertow in a surf zone, Coast. Eng. 8 (1984) 347–365.
[67] D. Swigler, P. Lynett, Laboratory study of the three-dimensional turbulence and kinematic properties associated with a solitary wave traveling over an alongshore-variable, shallow self, 2011, submitted for publication.
[68] C.E. Synolakis, The run up of solitary waves, J. Fluid Mech. 185 (1987) 532–545.
[69] M. Tissier, P. Bonneton, F. Marche, F. Chazel, D. Lannes, A new approach to handle wave breaking in fully non-linear Boussinesq models, Coast. Eng. 67 (2012) 54–66.
[70] V.V. Titov, C.E. Synolakis, Modeling of breaking and nonbreaking long-wave evolution and runup using VTCS-2, J. Waterw. Port Coast. Ocean Eng. 121 (1995) 308.
[71] M. Tonelli, M. Petti, Hybrid finite-volume finite-difference scheme for 2DH improved Boussinesq equations, Coast. Eng. 56 (2009) 609–620.
[72] M. Tonelli, M. Petti, Finite volume scheme for the solution of 2D extended Boussinesq equations in the surf zone, Ocean Eng. 37 (2010) 567–582.
[73] M. Tonelli, M. Petti, Simulation of wave breaking over complex bathymetries by a Boussinesq model, J. Hydraul. Res. 49 (2011) 473–486.
[74] M. Tonelli, M. Petti, Shock-capturing Boussinesq model for irregular wave propagation, Coast. Eng. 61 (2012) 8–19.
[75] G.D. Van Albada, B. Van Leer, W.W. Roberts, A comparative study of computational methods in cosmic gas dynamics, Astron. Astrophys. 108 (1982) 46–84.
[76] B. van Leer, Towards the ultimate conservative difference scheme V. A second order sequel to Godunov's method, J. Comput. Phys. 32 (1979) 101.
[77] J. Veeramony, I.A. Svendsen, The flow in surf-zone waves, Coast. Eng. 39 (2000) 93–122.
[78] G. Wei, J.T. Kirby, A time-dependent numerical code for extended Boussinesq equations, J. Waterw. Port Coast. Ocean Eng. 120 (1995) 251–261.
[79] G. Wei, J.T. Kirby, A coastal processes model based on time-domain Boussinesq equations, Research Report No. CACR-96-01, Center for Applied and Coastal Research, 1996.
[80] G. Wei, J.T. Kirby, A. Sinha, Generation of waves in Boussinesq models using a source function approach, Coast. Eng. 36 (1999) 271.
[81] T.-R. Wu, A numerical study of three dimensional breaking waves and turbulence effects, Ph.D. thesis, Cornell University, 2004.
[82] Y. Yamazaki, Z. Kowalik, K.F. Cheung, Depth-integrated, non-hydrostatic model for wave breaking and run-up, Int. J. Numer. Methods Fluids 61 (2009) 473.
[83] J.A. Zelt, The run-up of nonbreaking and breaking solitary waves, Coast. Eng. 15 (1991) 205–246.